공학석사 학위 논문

RuO_2-loaded TiO_2 nanotube array electrodes for efficient electrocatalytic gas evolution

이산화티타늄 나노튜브 어레이에 로딩된

이산화루테늄 전극의 전기화학적 기체발생 촉매특성

2018 년 8 월

서울대학교 대학원

재료공학부

허 성 은

RuO_2-loaded TiO_2 nanotube array electrodes for efficient electrocatalytic gas evolution

지도교수 김 진 영

이 논문을 공학석사학위논문으로 제출함

2018 년 8 월

서울대학교 대학원

재료공학부

허 성 은

허성은의 석사학위논문을 인준함

2018 년 6 월

위 원 장 _____ 남 기 태 _____ (인)

부 위 원 장 _____ 김 진 영 _____ (인)

위 원 _____ 장 호 원 _____ (인)

Abstract

RuO_2-loaded TiO_2 nanotube array electrodes for efficient electrocatalytic gas evolution

Seong Eun Heo

Department of Materials Science and Engineering

The Graduate School

Seoul National University

Ruthenium dioxide (RuO_2) has an advantage of various chemical reactions like dehydrogenation, gas phase oxidation of HCl, and chloro-alkali process. In order to enhance stability of RuO_2-based catalysts, the use of TiO_2 is successful in recent years. In general, nanostructured scaffolds with the large relative surface area are adopted in the catalytic reactions for maximizing the number of active sites. For the electrocatalytic reactions, however, the scaffold should be conducting enough so that the charges required for the redox reaction can be transported to the surface of the loaded RuO_2 catalysis. In the same context, TiO_2 nanotube arrays (NTAs) can be a promising scaffold for the CER

reaction, because it can transport charges (as evidenced in the solar cell or PEC applications) and it can be a good combination with RuO_2 (as evidenced by DSA®). In addition, the nanoscale morphologies (*e.g.* tube length, pore diameter, and wall thickness), crystalline structure (*e.g.* crystalline phase and preferred orientation), and the electrical properties (*e.g.* conductivity) can be precisely controlled by the processing parameters.

In this study, we firstly report the RuO_2-loaded TiO_2 NTAs as an efficient nanostructure electrode for the electrocatalytic CER process. Nanostructruring is well-known for enhancing the catalysts activity, we design TiO_2 based nanostructure to investigate more active catalysts. The samples have been prepared electrochemically (*i.e.* electrochemical anodization for preparing TiO_2 NTAs and electrochemical deposition for loading RuO_2) and the dependence of the CER performance on the materials properties of the composite electrodes such as the crystallinity and electrical conductivity have been investigated. It has been found that the conductivity of the electrode under the anodic polarization is essential for achieving good CER performance, and the black TiO_2 prepared by annealing as-anodized NTAs under an Ar atmosphere has been found to be the best scaffold for the RuO_2 catalysis.

keywords: Chlorine Evolution Reaction(CER), TiO_2 nanotube arrays (TiO_2 NTAs), Ruthenium dioxide, Heterogeneous Catalysis, Electrochemical analysis.

***Student Number*: 2016-29604**

Contents

List of Tables

List of Figures

Chapter 1. Introduction

1.1 Chlorine Evolution Reaction (CER)

1.1.1 Chlor-alkali process

The chlor-alkali industry for producing chlorine itself as a chemical is obviously one of the largest industrial electrochemical processes featured by the annual production of more than 70 million tons.[1-3] Besides the chlorine production, the CER is becoming more and more important for emerging applications based on the electrochemical advanced oxidation process such as the water purification,[4] sterilization,[5] and the ballast water treatment.[6] Also, chlorine gas is a gas used for various chemical reactions. It uses for synthesizing polyvinyl chloride (PVC), various chlorinated polymers (eg, polyvinylidene chloride (PVDC), Polychloroprene) and the precursor for various organic synthesis and inorganic synthesis.[4]

The chlor-alkali process is a process of electrolyzing brine to obtain chlorine gas and sodium hydroxide (NaOH). The following reactions occur at the cathode and anode.

Anode: $2Cl^- \rightarrow Cl_2 + 2e^-$ $E^0 = 1.3583\text{V}$ (vs. NHE)

Cathode: $2H_2O + 2e^- \rightarrow H_2 + 2OH^-$ $E^0 = 0.8277\text{V}$ (vs NHE) However, in the mercury cell, NaHg formation reaction ($2Na^+ + 2Hg + 2e^- \rightarrow 2NaHg$) occurs.

Overall: $2NaCl + 2H_2O \rightarrow Cl_2 + H_2 + 2NaOH$

Currently commercialized processes include mercury process, diaphragm process, and membrane process. The previous two processes are older than membrane processes and have been developed in Europe and the US, respectively. The membrane process is a process developed in Japan.[4] The schematic diagram for each process is as follows. (**Figure 1, 2, 3**)[7]

First, in the case of the diaphragm process, Na^+ is permeable to the asbestos layer to form NaOH. However, asbestos acts as a physical barrier between the two electrodes, allowing the movement of water and ions. Therefore, Cl^- ions in brine can be passed over to make NaCl, and OH-ions formed in the anode can be passed to the cathode to increase the pH, causing selectivity problems with Oxygen Evolution.

Second, in the mercury process, NaHg amalgam is formed instead of the reduction reaction of water in the reduction electrode. Because it is a membrane-free process, it can be driven at a high current density even if the voltage is the same. However, the use of mercury is decreasing due to pollution problems.

Third, there is a membrane process. The diaphragm process uses a membrane instead of asbestos, and the cation exchange resin, nafion, solves the NaCl impurity problem.

Chlor-alkali process is mainly carried out under the following conditions which is summarized in **Table 1**.[8] As can be seen in the table, it is an electrochemical process and therefore takes place at much higher temperature and current density conditions. Ruthenium-based catalysts, which are particularly stable and therefore far superior to other catalysts with stability, have been used predominantly.

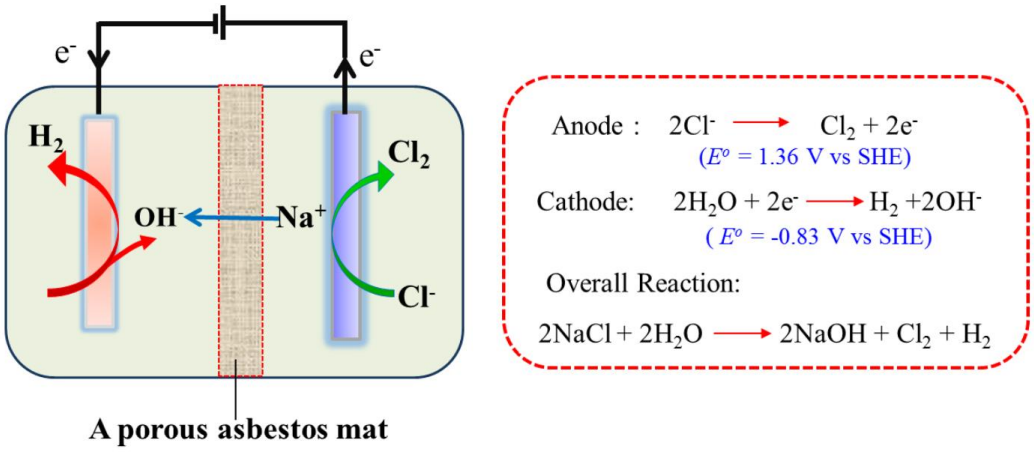

Figure 1. A schematic of the operation mechanism of the diaphragm cell. In the conventional diaphragm cell, a porous asbestos mat is used to separate the anodic reaction of CER and the cathodic reaction of HER, where NaOH is simultaneously formed in the cathodic compartment. [7]

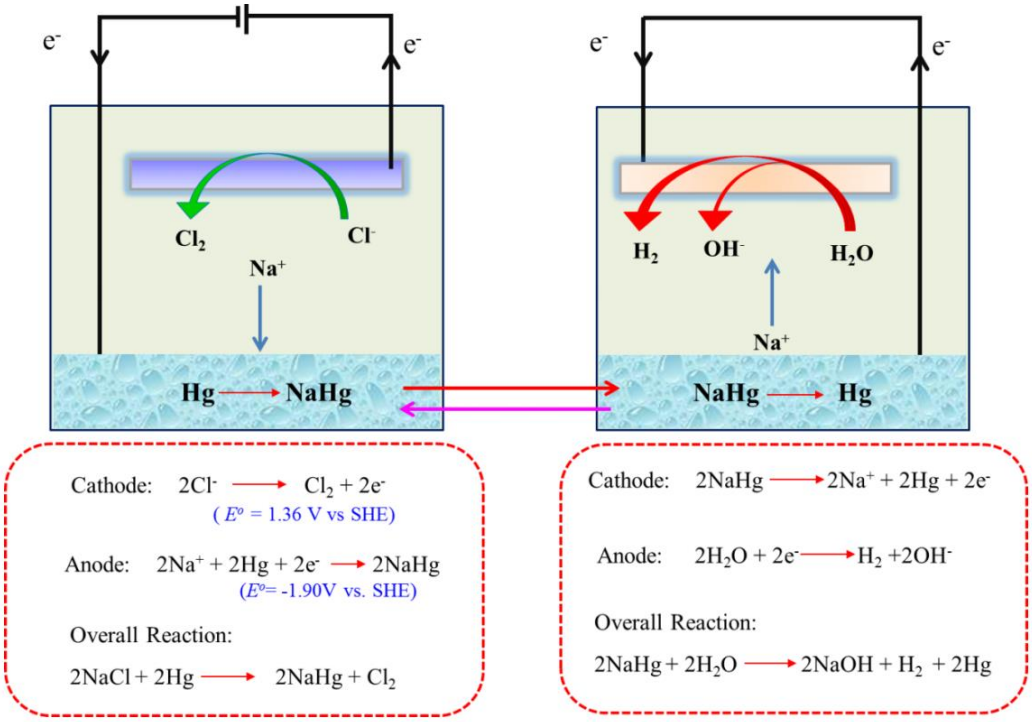

Figure 2. A schematic of the operation mechanism of the mercury cell. [7]

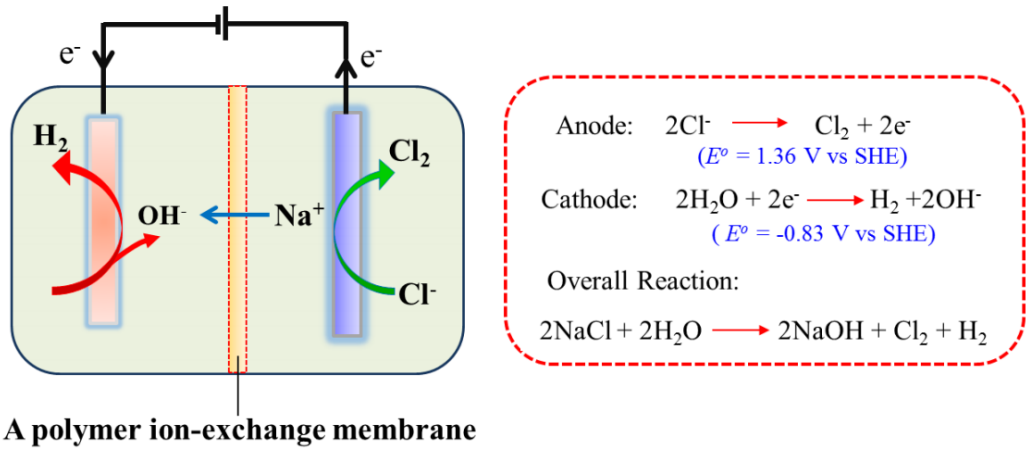

Figure 3. A schematic of the operation mechanism of the membrane cell. [7]

cell voltage (V)	2.4–2.7
current density (kA m^{-2})	1.5–7
temperature (°C)	90
NaCl concentration in the anolyte (g dm^{-3})	200
anolyte pH	2–4
NaOH concentration in the catholyte (wt %)	32

Table 1. Typical chlorine evolution reaction reaction conditions. [8]

1.1.2 Mechanism of chlorine evolution reaction

Chlorine evolution reaction can occur in various catalysts (RuO_2, IrO_2, PtO_2, etc.), and the mechanism has been mainly explored in the most successful RuO_2 or RuO_2-TiO_2 composite. So how does chlorine evolution occur on RuO_2 catalysts?

In recent years, Over group has explored what is happening on the single crystal RuO_2 (110) plane through various calculations and supported experimental evidence.[9-10] They argue that, as reported by other groups[11-12], the Tafel slope at low overvoltages and at high overvoltages are different and can be explained by first-principles calculations.

The crystal structure of RuO_2 is as follows. (**Figure 4**)[9] Among them, there are three kinds of sites that are considered as active sites of catalysts. First is the unsaturated Ru site(Ru_{cus}). As the oxidation progresses, Oxygen sticks to this, and the oxygen atoms protruding outward are called Oot. In the case of RuO_2, Oot is the main active site and is a catalyst capable of generating chlorine through two steps. The two steps are as follows.

1. Volmer step $O_{ot} + 2Cl^- \rightarrow O_{ot} - Cl + e^- + Cl^-$

2. Heyrovsky step $O_{ot} - Cl + Cl^- \rightarrow O_{ot} + Cl_2 + e^-$

The Volmer step is the process of making a reaction intermediate called OCl with Cl^- on the O_{ot}, and the Heyrovsky step is the process of finally producing the Cl_2 gas with Cl^- attached to the reaction intermediate. If the overvoltage is small, the second step (Heyrovsky step) is the step to determine the reaction rate (rate-determining step: RDS). However, if the overvoltage is large, the first step, the volmer step, determines the

reaction rate It is shown through thermodynamic calculation that it is a step. The change of the tafel slope according to the overvoltage is explained by various methods such as the amount of Cl on the surface. However, the calculation shows that the RDS changes depending on the overvoltage. (**Figure 5)**[10]

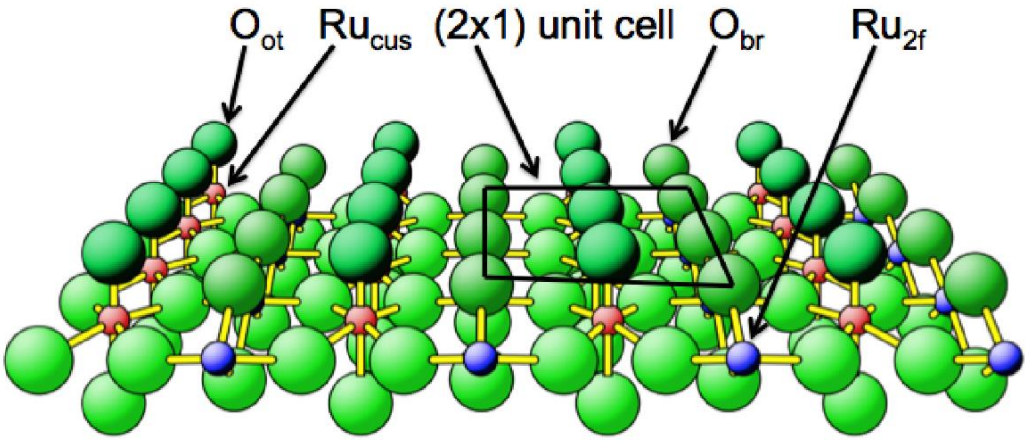

Figure 4. (2×1) surface unit cell of RuO_2(110). Undercoordinated ruthenium atoms of the RuO_2(110) surface are denoted by Ru_{cus} and Ru_{2f}. Adsorbates bridging two Ru_{2f} atoms are indicated with the index "br" and adsorbates in terminal position on Ru_{cus} atoms with the index "ot" (on-top). red spheres: ruthenium 1-fold cus atoms (Ru_{cus}), blue spheres: ruthenium 2-fold cus atoms (Ru_{2f}), green spheres: oxygen atoms. [9]

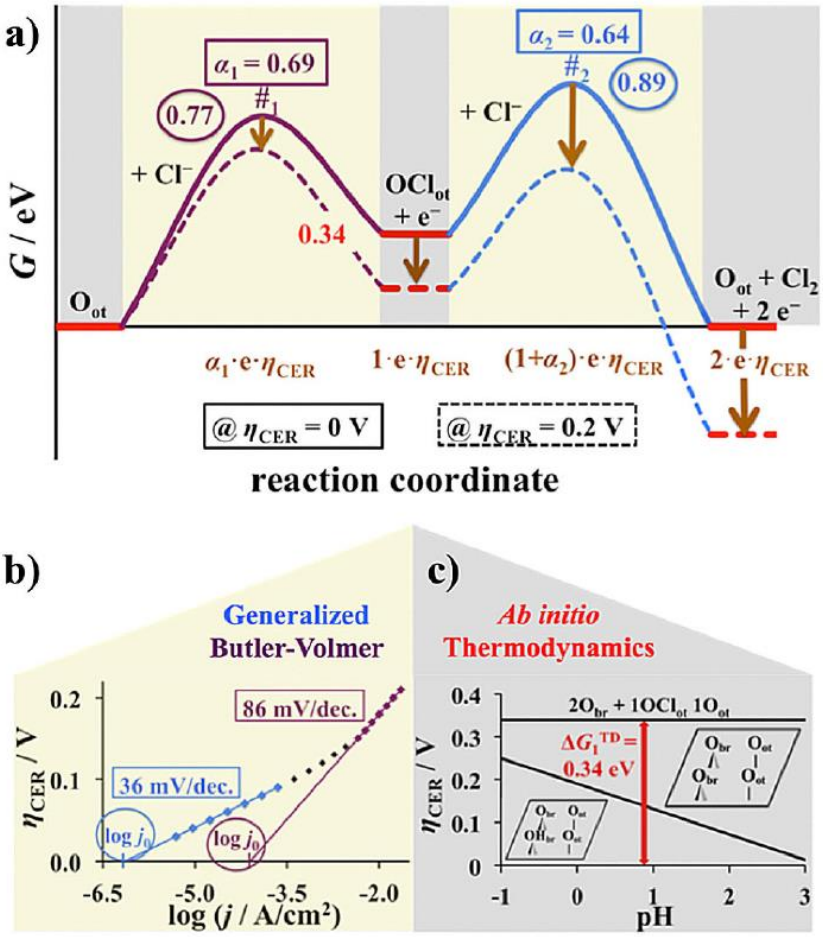

Figure 5. a) the free-energy profile along the reaction coordinate at different applied overpotentials. ($\eta_{CER} = 0V, 0.2V$, respectively) b) Experimental Tafel plot for a wide range of overpotentials, exhibiting two characteristic linear Tafel regions with Tafel slopes of 36 and 86 mV/dec. c) Ab initio thermodynamics provides the Pourbaix diagram that summarizes the stable surface configurations depending on the pH value and the applied overpotential. Under CER conditions, a fully-oxygen covered RuO_2(110) surface is energetically preferred. [10]

1.1.3 Recent research trend and literature review

Ruthenium oxide (RuO_2) has been known as one of the best heterogeneous catalysis for the anodic chlorine evolution reaction (CER). In spite of the excellent catalytic properties, however, the biggest issue of the RuO_2-based catalysis is the high materials cost. Therefore, the commercial CER catalysis widely used in the industry is the Dimensionally Stable Anodes (DSA®) consisting of 70-mole% rutile TiO_2 and 30-mole% RuO_2, which exhibits minimal loss of performance with minimal use of RuO_2. In addition, the presence of TiO_2 has been known to enhance the stability under the anodic polarization during the CER process.[13-14]

Research Trends

In the case of CER, much research has been done on mechanisms.[15-16] Various mechanisms have been proposed (**Table 2**)[17] and recent studies have shown that thermodynamic calculations and first principles can better explain experimental results. In addition, many studies on selectivity have been carried out since Cl_2 chemistry can cause various chemical species to proceed in aqueous solution (**Figure 6**)[8], and the problem of oxygen generation at the oxidation electrode always follows. Surprisingly, selectivity is also closely related to stability. As the selectivity to Cl_2 increases, there is less current associated with OER, which leads to slower degradation of the oxide and improved stability. There are two major factors that affect selectivity.[8] First, it is a process condition (pH, temperature, the current density of the electrolyte, the Cl^-concentration

of the electrolyte, etc.). The second is the structure and composition of the anode. Various studies have confirmed that selectivity and efficiency are affected by what anode is, what doping is, what amount of Ru is, and so on. The results are summarized as follows.

1. The partial current of OER can be significantly lowered in the case of an electrolyte added with HCl.[18-19]

2. The lower the pH, the more kinetics of OER are inhibited. Therefore, it is preferable to measure in acidic conditions.[20]

3. The higher the Cl^- concentration, the better the current efficiency.[21] This can be explained by the increase of adsorption due to mass transfer enhancement.

4. The higher the current density, the lower the selectivity.[20]

5. When the pH is low in the Cl^--rich electrolyte, the formation of soluble chloride is closely related to degradation.[22] However, if the pH is higher (base condition), there seems to be a different degradation mechanism.

6. The corrosion of DSA is minimum between pH = 2 and 3.[19] This can be explained by the pourbaix diagram (**Figure 7**).[23] Because conversion from RuO_2 to RuO_4 is important to explain degradation mechanism.

7. The factor related to the stability of DSA is the OER partial current. The higher the partial current of OER, the more Ru oxidation and corrosion increases.[8] The degradation mechanism of RuO_2 associated with OER is shown in the figure below. (**Figure 8**) [24] As

the anodic polarization is overprotected, $RuO(OH)_2$ formed on the surface is converted into RuO_4^{2-}, and the amount of Ru is gradually decreased. However, the current density of CER and stability of electrode were not related to each other.[8] It is not a problem that the current density of the CER increases, but the occurrence of other side reactions such as OER is a key factor in deterioration.

8. It has been reported that as the active surface increases, local current density decreases and selectivity increases.[21] The surface area was mainly controlled by the size control of RuO_2 particles. In this study, the TiO_2 nanotube array was used to increase the active surface.

9. It can be seen that the selectivity of OER increases as the loading amount of the catalyst increases.[21]

10. Other materials besides RuO_2 have also been reported for CER activity. IrO_2[25], PdO[26], and CoOx[27] is mainly investigated. In addition, RuO_2 composite materials containing SnO_2[28], Sb_2O_5[29-30], and TiO_2[31] have been reported. In the case of RuO_2, TiO_2 was found to be advantageous in terms of cost and stability, but the pure phase was more advantageous in the case of IrO_2. PdO has not been explored much, but it has proved to be more advantageous than RTO (RuO_2-TiO_2 mixed oxide) in terms of stability and efficiency. As CoOx has been reported as a good catalyst for OER, it has poor selectivity compared to other materials, and there is even corrosion due to decomposition of HClO (hypochlorite decomposition). Due to the high price of Ru-based materials, substitution with non-noble

metals such as Co has been studied extensively, but there has not yet been a successful case of Ru over Ti-mixed RTO.

11. In addition to changing materials, many attempts have been made to change the electronic sturucture through doping. In particular, there have been many attempts to improve selectivity by doping various elements such as Zn[32-33], Ni[34], Mg[35], Fe[36], Co[27] and Sn[36] into RuO_2.

12. As a result, the RTO composition of RuO_2 mixed with TiO_2 has more advantages in terms of activity, selectivity, stability, and cost than other catalysts.

13. In recent years, processes using catalysts using Mn-based cheap materials have been introduced in academia, eliminating membranes.[7] **(Figure 9**)

No.	Mechanism	Author	Year
(1)	$2Cl^- \rightleftarrows Cl_2(surf) + 2e^-$ $Cl_2(surf) \rightarrow Cl_2(bulk)$	R. G. Erenburg, L. I. Krishtalik et al.	1972 [27]
(2)	$Cl^- \rightleftarrows Cl_{ad} + e^-$ $2Cl_{ad} \rightarrow Cl_2$	G. Faita and G. Fiori	1972 [38]
(3)	$Cl^- \rightleftarrows Cl_{ad} + e^-$ $2Cl_{ad} \rightarrow Cl_2$ and $Cl_{ad} + Cl^- \rightarrow Cl_2 + e^-$	R. G. Erenberg, L. I. Krishtalik et al.	1972 [50]
(4)	$Cl^- \rightleftarrows Cl_{ad} + e^-$ $Cl_{ad} \rightarrow (Cl_{ad})^+ + e^-$ $(Cl_{ad})^+ + Cl^- \rightleftarrows Cl_2$	R. G. Erenberg, L. I. Krishtalik et al.	1975 [36]
(5)	$Cl^- \rightleftarrows Cl_{ad} + e^-$ $Cl_{ad} + Cl^- \rightarrow Cl_2 + e^-$	L. J. J. Janssen et al.	1977 [51]
(6)	$RuO_2 + H_2O \rightarrow RuO_3 + 2H^+ + 2e^-$ $RuO_3 + Cl^- \rightarrow RuO_2(ClO_{ad})^-$ $(ClO_{ad})^- + Cl^-_{ad}$ (or Cl^-) $+ 2H^+ \rightarrow Cl_2 + H_2O$	J. Augustynski et al.	1978 [40]
(7)	$Cl^- \rightleftarrows Cl_{ad} + e^-$ $H_2O \rightarrow OH + e^-$	D. A. Denton, J. A. Harrison et al.	1979 [52]
(8)	$O_{ad} + Cl^- \rightarrow OCl_{ad} + e^-$ $OCl_{ad} + Cl^- \rightarrow O_{ad} + Cl_2 + e^-$	L. K. Burke and J. F. O'Neill	1979 [45]
(9)	$(M^z) \rightleftarrows (M^{z+1}) + e^-$ $(M^{z+1}) + Cl^- \rightarrow (M^{z+1})Cl_{ad} + e^-$ $(M^{z+1})Cl_{ad} + Cl^- \rightleftarrows (M^z) + Cl_2$	L. I. Krishtalik	1981 [46]
(10)	$H_2O \rightleftarrows OH_{ad} + H^+ + e^-$ $M\text{-}OH_{ad} + Cl^- \rightarrow M(OH)Cl + e^-$ $HOCl + HCl \rightleftarrows Cl_2 + H_2O$	L. I. Krishtalik and R. G. Erenburg	1981 [41]
(11)	$M\text{-}OH_2^+ \rightleftarrows M\text{-}OH + H^+$ $M\text{-}OH \rightleftarrows M\text{-}O + H^+ + e^-$ $M\text{-}OCl + Cl^- + H^+ \rightleftarrows M\text{-}OH + Cl_2$ or $M\text{-}OCl + Cl^- \rightleftarrows M\text{-}O + Cl_2 + e^-$	R. G. Erenburg	1984 [53]
(12)	$O_{ot} + Cl^- \rightarrow O_{ot}\text{-}Cl^- + 2e^-$ or $O_{br} + Cl^- \rightarrow O_{br}\text{-}Cl^+ + 2e^-$	T. Hepel et al.	1986 [44]
(13)	Cl_2 diffusion limitation	V. V. Losev et al.	1989 [35]
(14)	$M^Z + H^+ \rightleftarrows MH^{Z+1}$ $M^Z \rightleftarrows M^{Z+1} + e^-$ $M^{Z+1} + Cl^- \rightleftarrows MCl^{Z+1} + e^-$ $MCl^{Z+1} + Cl^- \rightleftarrows M^Z + Cl_2$ $2MCl^{Z+1} \rightleftarrows 2M^{Z+1} + Cl_2$	J. L. Fernandez et al.	2002 [47, 54, 55]
(15)	Radical spillover mechanism	S. Ferro et al.	2002 [17]
(16)	RuO_2 nanocrystals	J. Jirkovsky et al.	2006 [16]
(17)	$M^Z\text{-}OH_2^+ \rightleftarrows M^{Z+1}\text{-}OH + H^+ + e^-$ $M^{Z+1}\text{-}OH + Cl^- \rightleftarrows M^{Z+1}\text{-}OHCl + e^-$ $M^{Z+1}\text{-}OHCl + Cl^- + H^+ \rightleftarrows M^Z\text{-}OH_2^+ + Cl_2$ $M^{Z+1}\text{-}OHCl + Cl^- \rightleftarrows M^{Z+1}\text{-}OH + Cl_2 + e^-$	M. Thomassen et al.	2006 [48]
(18)	pH dependence in different surface orientation	E. Guerrini, S. Trasatti	2006 [42]
(19)	$O_{ot}\text{-}O_{ot} + 2Cl^-_{(aq)} \rightarrow (O_2)_{ot}\text{-}Cl + Cl^- \rightarrow O_{ot}\text{-}O_{ot} + Cl_2(g) + 2e^-$	H. A. Hansen et al.	2010 [29]

Table 2. Various mechanisms proposed for chlorine evolution reaction. [17]

species	name	Cl oxidation state
Cl^- (aq)	chloride (ion)	−1
Cl_3^- (aq)	trichloride ion	−1, 0
HCl (g) or (aq)	hydrochloric acid	−1
Cl_2 (g) or (aq)	chlorine gas	0
HOCl (aq)	hypochlorous acid [or chloric (I) acid]	+1
ClO^- (aq)	hypochlorite (ion) [or chloric (I) ion]	+1
Cl_2O (g)	chlorine monoxide	+1
$HClO_2$ (aq)	chlorous acid	+3
ClO_2^- (aq)	chlorite (ion)	+3
ClO_2 (g)	chlorine dioxide	+4
ClO_3^- (aq)	chlorate (ion)	+5
ClO_4^- (aq)	perchlorate (ion)	+7

$$Cl_2 + H_2O \leftrightarrow H^+ + HOCl + Cl^-$$

$$HOCl + H_2O \leftrightarrow H_3O^+ + ClO^-$$

$$2HOCl + ClO^- \leftrightarrow {ClO_3}^- + 2H^+ + 2Cl^-$$

Figure 6. Various chlorine species during chlorine evolution and three main reactions in chlorine chemistry. [8]

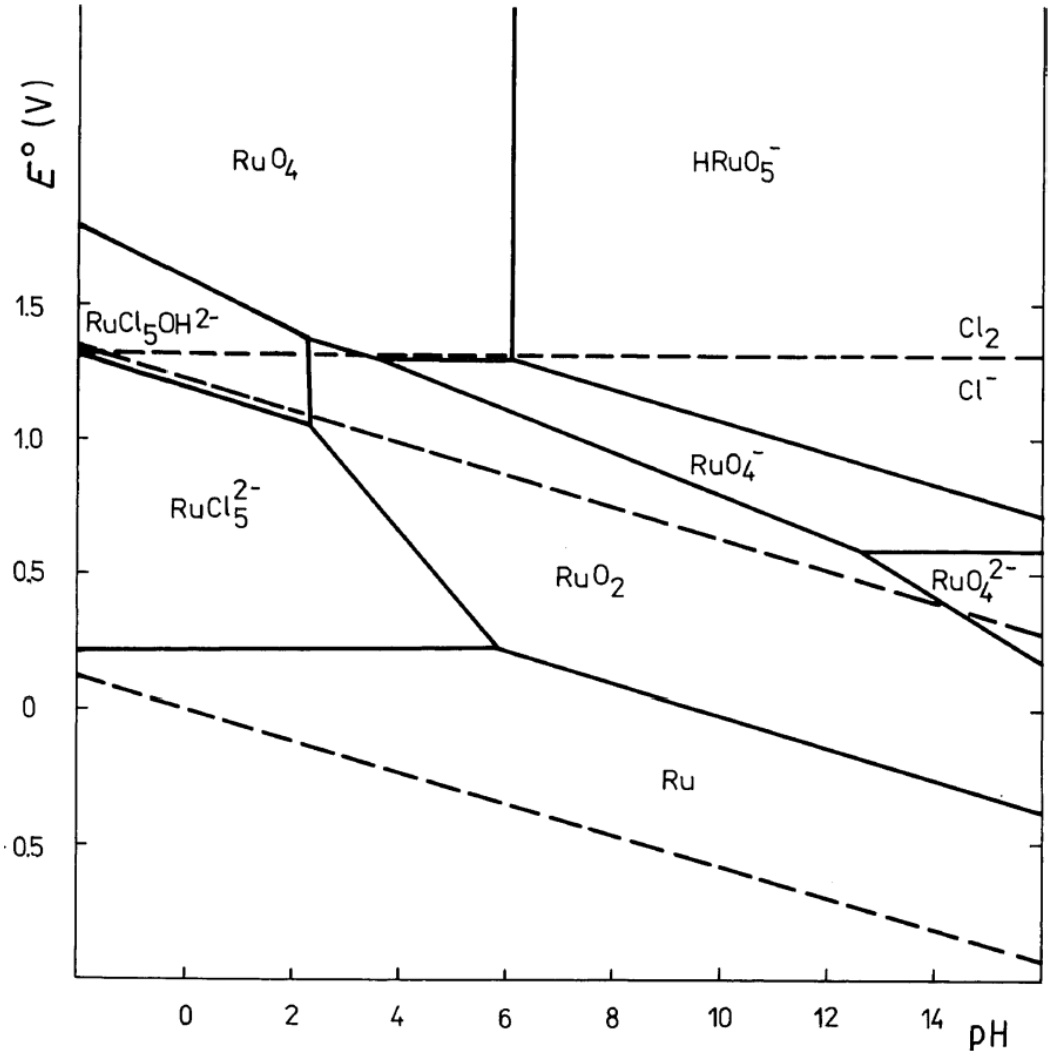

Figure 7. Pourbaix diagram for ruthenium in concentrated NaCl solution (25°C, 265g/dm^3 NaCl). [23]

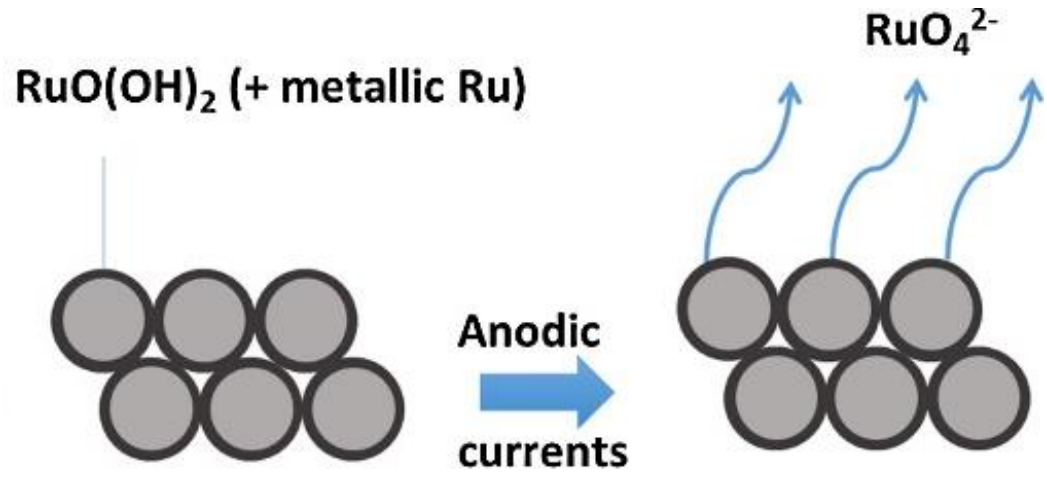

Figure 8. Corrosion of RuO_2-based materials under anodic current. [24]

factor	selectivity for oxygen evolution	refs	comment
modified composition	decrease	36, 158, 162, 167, 169, and 173	several modified coatings exist
increased surface area	increase	69	related to decrease in j_{loc}?
larger coating crystallite particle size	decrease	78	related to increase in j_{loc}?
higher oxide loading	increase	75	
less Ru in RTO coating	decrease	67, 68, 75, 139, 154, 161, and 171	same effect as decreased j_0 for reaction 11? Connected to increased chlorate formation[36,141,150,154]
decreased j_0 for reaction 11	decrease	69, 150, 159, and 167	but reaction 11 not only source
IrO_2 substitution	decrease?	74	doped into RTO; dorrosion products might increase selectivity in practice
Co substitution	decrease?	78	doped into RuO_2;[82,83,189] saw increase
SnO_2 substitution	decrease	69, 71, 147, and 172	doped into RuO_2[69,172] or together with Pd[71]
HfO_2 substitution	increase	69	doped into RuO_2
Zn substitution	increases	181, 182, and 189	doped into RuO_2
Ni substitution	decrease	77	doped into RuO_2
Mg substitution	decrease	193	doped into RuO_2
Fe substitution	decrease?	180	doped into RuO_2, high Cl_2 selectivity in Ar-saturated solutions
overlayer material	decrease	60	overlayer of Pt mixed with IrO_2
support material	possible effect	8 and 179	

Table 3. Summary of RuO_2-based composite materials activity and selectivity. [8]

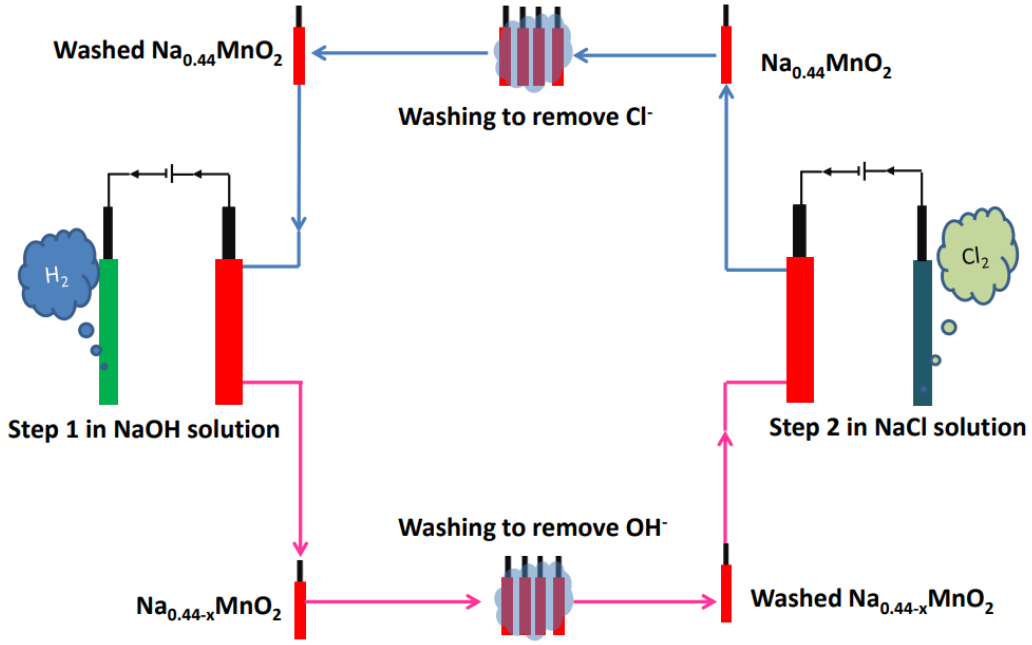

Figure 9. conceptual process scheme of the novel two step chlor-alkali process. [7]

1.2 TiO_2 nanotube arrays (TiO_2 NTAs)

1.2.1 Brief outline of TiO_2

Titanium dioxide (TiO_2) is widely investigated due to its good stability (including corrosion resistance) and physical properties and biocompatibility. Especially, it is widely used in pigment[37], sunscreens[38-39], paints[40], ointments, and toothpaste[41]. In energy-related application, Fujishima and Honda first reported as the photocatalytic splitting of water under UV light.[42] In chlorine evolution reaction, the presence of TiO_2 has been known to enhance the stability under the anodic polarization during the CER process.[13-14] In addition, TiO_2 is often used as an additive in conjunction with SnO_2 to enhance the selectivity of CER with respect to oxygen evolution reaction (OER).[20] In fact, it has been reported that up to about 70% TiO2 increases selectivity rather than impairing the catalytic properties of RuO_2. This is because TiO_2 lowers the partial current due to OER which may prevent dissolution.[13-14]

TiO_2 often has four polymorphs. tetragonal rutile, tetragonal anatase, orthorhombic brookite, and monoclinic TiO_2.[43] (**Figure 10**) In addition, polymorphs at high pressure, or less common structrue have been reported as well.[44] Of these, rutile is the most thermodynamically stable phase formed at high temperatures[45], while the remainder is formed at a slightly lower temperature. TiO_2 nanotube arrays are amorphous in the as-dep condition[46] and can be transformed to anatase or rutile when annealed.[47] But for rutile, it needs to be heat treated at very high temperatures (> 800℃).[47] Although it has

been reported that when the heat treatment is performed at a temperature of 900℃ or higher, the TiO_2 nanotube array is completely changed to rutile, but the shape of the TiO_2 nanotube array is not maintained.[47] Not only TiO_2 nanotube arrays, Mo oxide nanotube arrays have also been observed to break the shape of nanotubes during high-temperature heat treatment.[48] This is because the crystal structure is changed and lattice strain is generated and thus strain is generated. In addition, rutile is the most thermodynamically stable phase in the bulk system[45], but at the nanoscale, many experimental and theoretical studies support that the most stable phase is anatase.[49] Therefore, in the case of TiO_2 nanotube arrays, many studies related to anatase have been conducted.

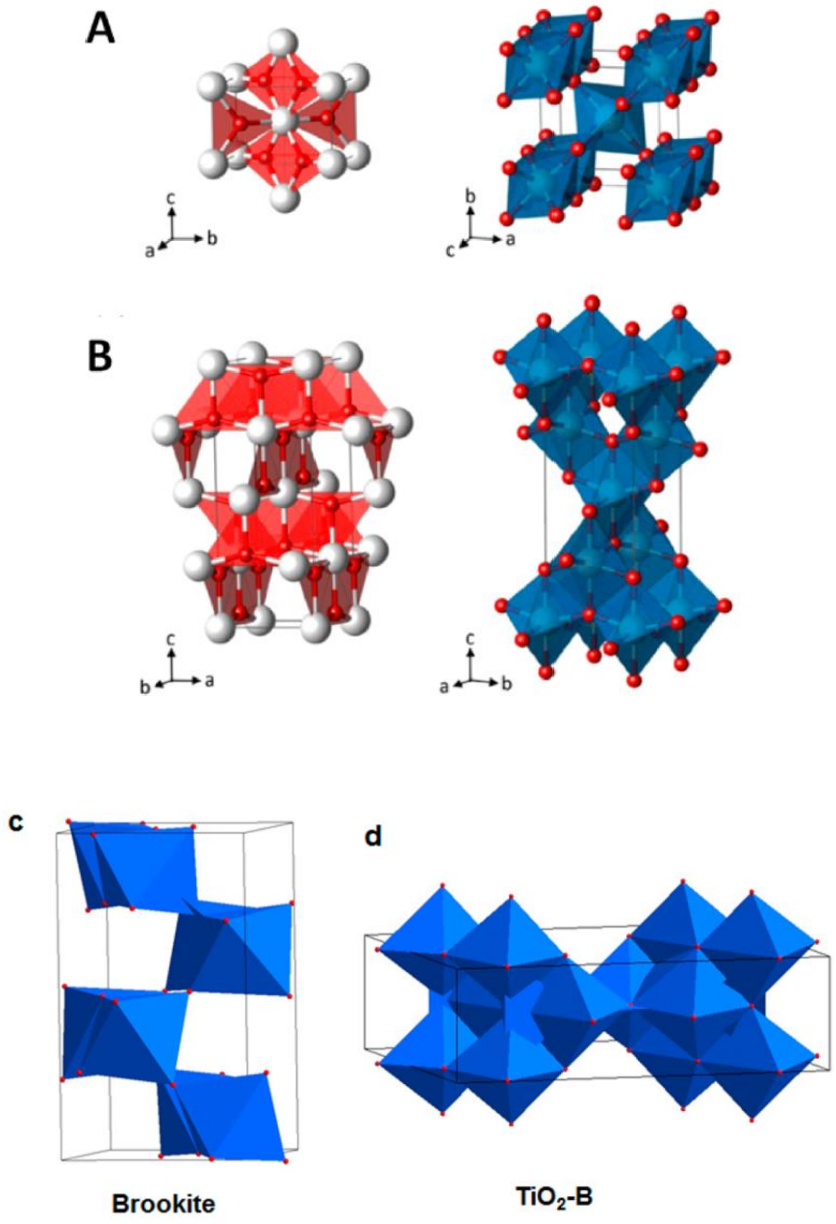

Figure 10. polyhedral representation of rutile(A) and anatase(B) and other unit cell structure (brookite: c, TiO_2-B: d) [50-51]

1.2.2 Self-organized TiO_2 Nanotube arrays

There are many ways to make TiO_2 nanotubes. (**Figure 11**) It can be divided into solution-based approaches, vapor-based approaches, templated growth and electrochemical methods.[50] Solution-Based Approaches include hydrothermal/solvothermal methods, sol-gel methods, surfactant-assisted methods, microwave assisted methods, sonochemical synthesis, high temperature pyrolysis and electrospinning methods. Solution-based approach is low cost, and simple process, but it still has a disadvantage that it is not easy to control morphology or control physical properties.[50] Vapor-based approaches include chemical / physical Vapor Deposition (CVD / PVD), atomic layer deposition(ALD)-related methods, and pulsed laser deposition. Since it grows at a high temperature in a vacuum condition, it has good crystallinity and it is a great advantage that it can precisely control composition and growth site with a catalyst or a precursor.[50] However, it has a disadvantage of being expensive and having a bad scalability. Templated growth is a method of controlling morphology by using a porous template. The biggest advantage is that growth does not have a large effect on the crystal surface of the material. However, there is a disadvantage that crystallinity is not good and purity is not easy to control. Electrochemical methods can grow TiO_2 nanotube arrays directly on Ti metal, and it is not difficult to control length or pore size. Many people have tried it because it is simple, low-cost, and excellent in scalability.

The origin of the electrochemical process of forming TiO_2 nanotube arrays dates back to the formation of the Alumina porous layer. Anodic Aluminum Oxide (AAO) was

first reported by Rummel[52] and Baumann[53], and has attracted much interest from researchers. Especially, various anodization methods (mild anodization (MA), hard anodization (HA), pulse anodization (PA), cyclic anodization (CA)) have been studied, especially for templates or platform as energy storage[54-56], photovoltaic [57-58], photonic applications[59-60], biomedical applications[61-62], etc.). In 1999, Zwilling and co-workers demonstrated that TiO_2 nanotube arrays can be synthesized for the first time using fluorine-containing electrolytes.[63] The formation of nanotube arrays in this manner has also been applied to other valve metals and alloys (Hf[64], Ta[57], W[65], Nb[66], Zr[67], Fe[68], Mo[48], TiW[69] etc).

A simple mechanism for making TiO_2 nanotube arrays is as follows. (**Figure 12**)[70]

Working Electrode (Anode): $M \rightarrow M^{z+} + ze^-$

$2H_2O \rightarrow O_2 + 4H^+ + 4e^-$ (Oxygen evolution reaction: OER)

$M + \frac{z}{2}H_2O \rightarrow MO_{z/2} + zH^+ + ze^-$ (formation of oxide)

Counter Electrode (Cathode, Pt or carbon): $2H^+ + 2e^- \rightarrow H_2$ (Hydrogen evolution reaction: HER)

Oxidation takes place at the working electrode, leading to a change from pure metal to metal oxide. At the counter electrode, reduction occurs, so hydrogen ions contained in the electrolyte are reduced and hydrogen gas is observed. Depending on various electrolyte conditions (temperature, pH, applied potential, electrolyte or organic, fluoride contents, viscosity, etc.), the kinetic of the reactions occurring on the working electrode can be controlled, It plays a key role. There are three possible scenarios for the growth of the oxide depending on the conditions of the electrolyte. (**Figure 12**)[71]

Scenario 1: If oxide is completely dissolved in the electrolyte, electropolishing of the metal layer will be observed.

Scenario 2: If oxide does not dissolve in electrolyte at all, compact oxide is formed.

Scenario 3: If the oxide partially dissolves in the electrolyte, the M^{z+} cation can be solvated Under certain conditions the formation and dissolution of the oxide will be in a steady state to form a nanotube or porous layer.

The current of anodization can be obtained by using a high field approximation, and the ionic current density is determined by the thickness of the barrier. The growth of the oxide depends on the rate at which the M^{z+} ions migrate outward and the O^{2-} ions moving inward from the water to the metal. (**Figure 12**) In general, the growth of oxide is related to the magnitude of the electric field, and the equation is given by

$$I = Ae^{BE}, E = \frac{\Delta U}{d}$$

where I is the current, ΔU is the voltage across the oxide layer of thickness d, and A and B are material-dependent constants.[72]

If a compact oxide is formed, the electric field is greatly reduced as the thickness of the oxide layer becomes thicker, which interferes with ion migration, and the growth of the oxide is stopped at any moment. This is given by d = 2.5 nm / V * U in TiO_2.[73]

As in Scenario 3, when the oxide partially melts, metal cations will form with F anions and solvated to form water-soluble MF^{6-}. When these chemical solvents and oxides form a steady state, a porous film is formed.

Generally, a hexagonal nanopore cell (honeycomb structure) is formed in a TiO_2 nanotube array. How does the nanotube form? This is related to the chemical nature of TiF^{6-}. First, the F-ion is smaller, so it can diffuse faster than the larger O^{2-}ion. Because of this, an F-rich layer is formed at the metal / oxide interface and a tube shape is formed as water easily dissolves these layers. In contrast, in the case of Al, Al-fluoride is not well soluble in water, so a porous form is better formed.

1.2.2.1 Factors affecting the morphology of TiO_2 NTAs

1. H_2O-based (aqueous) vs. organic-based

In the case of H_2O-based electrolytes, the chemical etching rate is faster than the organic-based ones, so the steady state is reached sooner and the length is limited. The maximum growth is reported to be about 2.5 micrometers.[74] On the other hand, an organic-based electrolyte can grow up to 100 micrometers, and the pore radius can grow larger.[75] In addition, organic-based electrolytes can slow the dissolution of cell boundaries because the chemical etching rate is significantly slower, which is advantageous for making highly ordered structures. The nature of the organic material also depends on whether it is based on dimethyl sulfoxide (DMSO) or on ethylene glycol (EG). Single-walled NTAs are created based on DMSO[76], whereas double-walled NTAs are created based on EG.[47] (**Figure 13**)

2. Temperature

Growth occurs more slowly because the kinetic associated with ion migration is worse at lower temperatures. In addition, if the temperature is very low, it can be observed that the nanotubes are grown not in nanotubes but in chemical etching.[77] As a result of the observation of the composition, the nanocolumn is composed of an F^-rich composition and is easily etched by water. (**Figure 13**)

3. Presence or absence of complexing agent

When complexing agents such as lactic acid[78] or EDTA[79] are used, Ti^{4+} ions are caught, which prevents Ti^{4+} ions from diffusing into the inner wall. As a result, the thickness of the bottom layer becomes thinner and the thickness of the barrier oxide becomes thinner, so that a higher electric field is required than usual. So we can observe a phenomenon that grows longer than when no complexing agent is added. In addition, dielectric breakdown is not observed at a relatively large voltage. (**Figure 13**)

4. Concentration and pH of F^- ion

The concentration of F ion and pH are also related to the dissolution of the oxide layer. The lower the pH, the faster the dissolution rate. Also, the higher the concentration of fluoride, the faster the dissolution rate of the oxide layer.[80] (**Figure 13**)

5. aging effect

As the anodization progresses more and more, the TiF^{6-}complex is formed in the electrolyte, which increases the ionic concentration and increases the conductivity of the electrolyte.[81] As a result, the longer the length of the TiO_2 nanotubes is, the longer the anodization is repeated. In addition, the increased TiF^{6-} concentration has the effect of slowing the rate of chemical dissolution and increasing the maximum oxide length.[82] (**Figure 13**)

6.Voltage

Voltage is often known to have a proportional relationship with diameter.[83] Higher voltages increase the strength of the electric field through the oxide layer and affect the migration and diameter of the ions. However, if the electric field reaches a certain threshold value, the diffusion of water becomes a rate-determining step and the voltage and potential are inversely proportional to each other. (**Figure 13**)

7. Time

The length of the TiO_2 nanotubes can be controlled with time, and the maximum length of the TiO_2 nanotubes is determined by the steady state. Sometimes it takes a long time to observe the shape of the nanograss.[80] (**Figure 13**)

8. Presence of pre patterning

If you do pre-patterning, you can observe that the tube grows in a more well-ordered form.[84] The most common method is the double anodization method, which is also derived from AAO growth. [85] In addition, pre-patterns can be created using Focused Ion Beam (FIB)[86] or other nanoimprinting methods such as stamping.[87] (**Figure 13**)

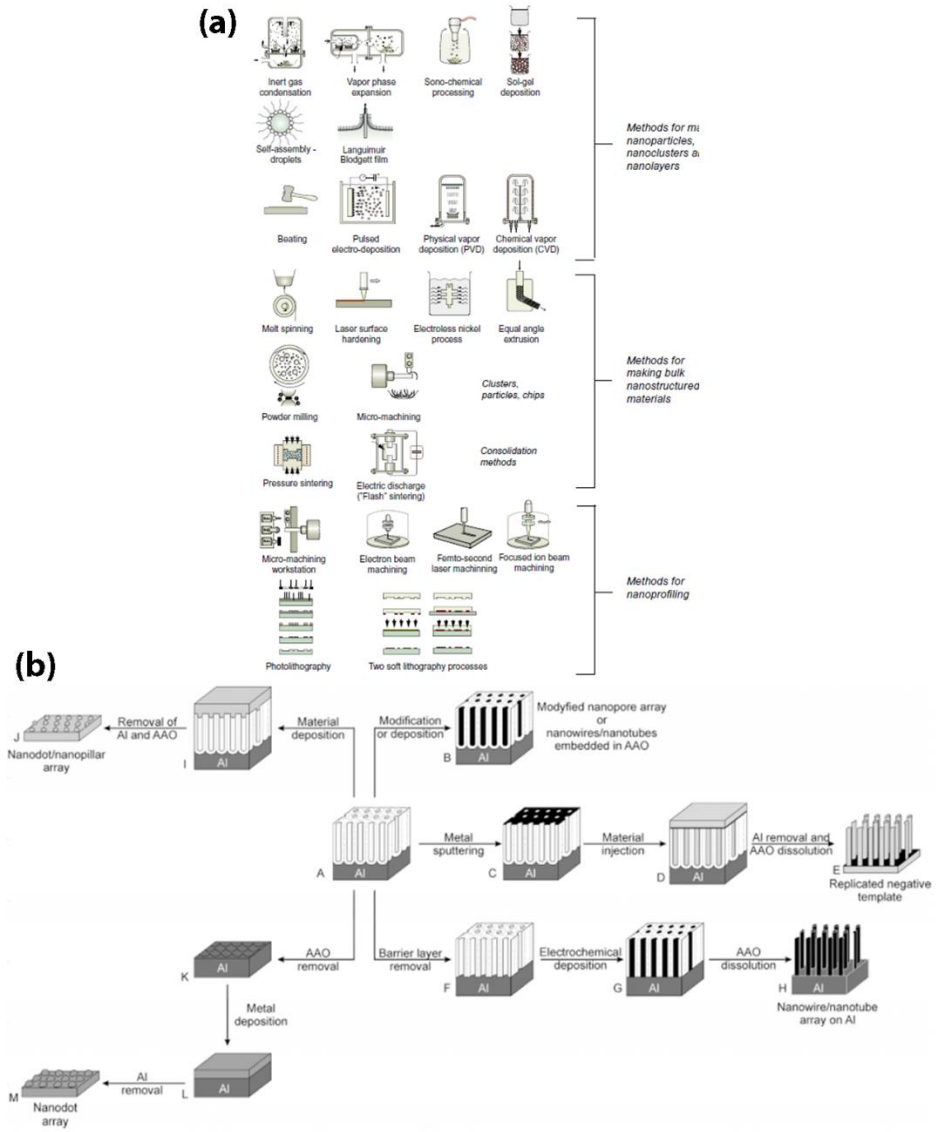

Figure 11. Summary of synthesize methods for TiO_2 nanomaterial. (a) general method for synthesizing nanomaterials [88] (b) AAO- assisted templated synthesize. [89]

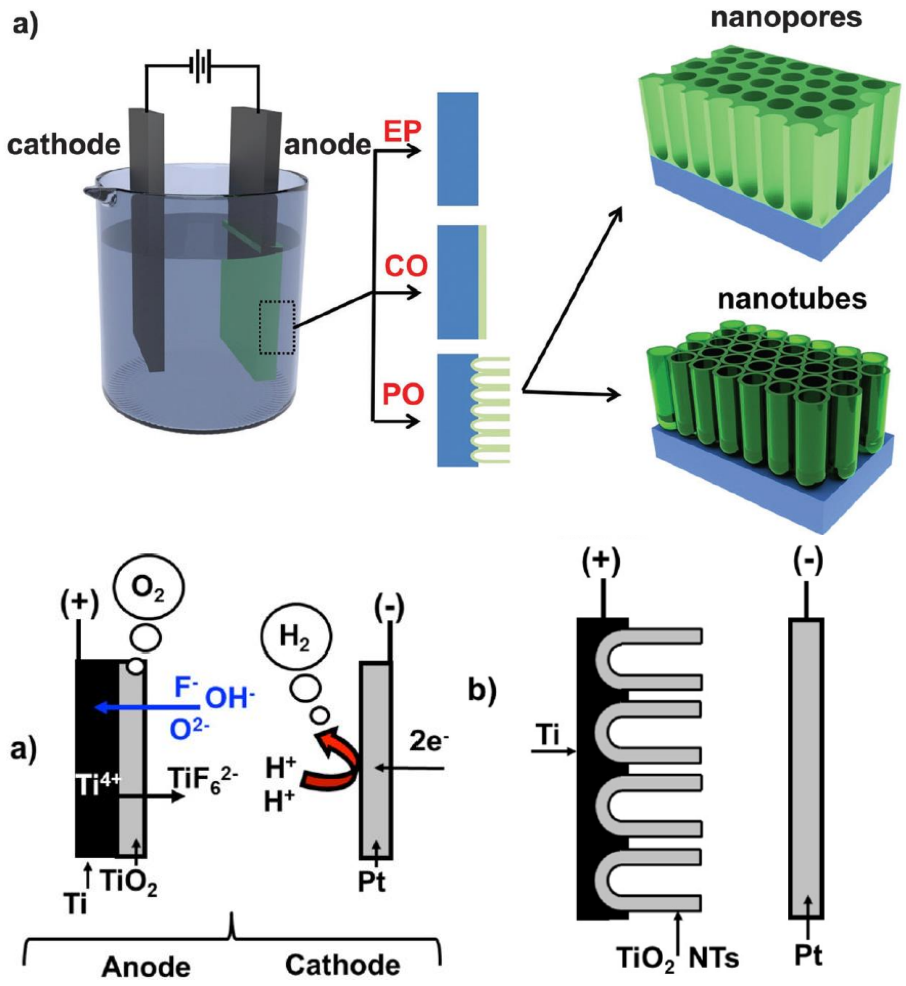

Figure 12. Three possible scenarios for electrochemical anodization schematic view of reactions that occur during the anodization. [70-71]

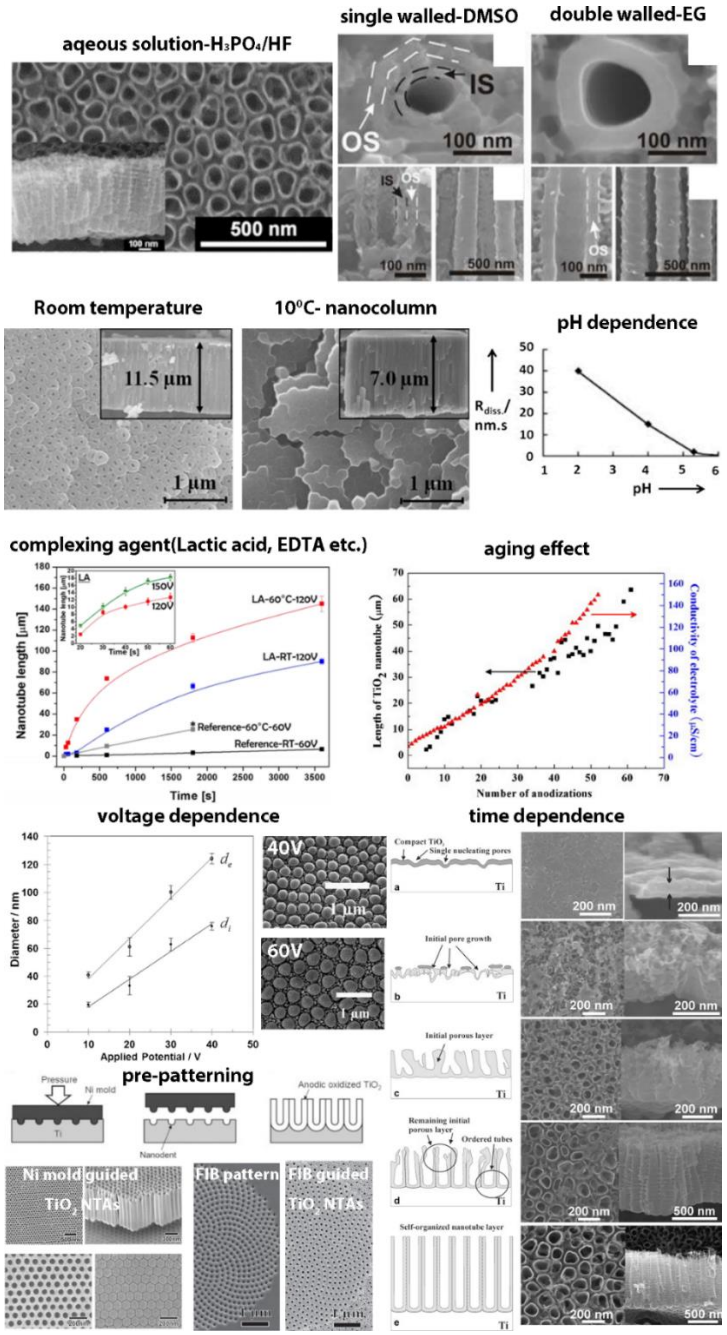

Figure 13. Factors that affect the morphology of TiO_2 nanotube arrays [75, 77, 90, 78, 80, 86, 87]

1.2.3 Mechanistic regime

There are two main mechanisms that explain the formation of TiO_2 nanotube arrays. (**Figure 14**)[70] One is the field-assisted dissolution model and the other is the flow mechanism model. The field-assisted dissolution model describes that the oxide layer is formed in both the metal / oxide interface and the oxide / electrolyte after the pore is first initiated, and the electric field is concentrated inside the pore, causing dissolution centering thereon Model. Recently, the flow mechanism model has been proposed to explain other phenomena. The pore initiation of TiO_2 nanotube arrays differs slightly depending on the type of electrolyte. In the case of aqueous solution, both Ti^{4+} injection into the electrolyte and dissolution of the oxide layer by F^- ion contribute to the electrolyte, whereas in the organic solvent, the chemical dissolution becomes very small and the pore is formed only under special circumstances. Recent studies have reported that morphological instability leading to pore initiation and self-order occurs in certain oxide formation efficiencies. In this model, plastic flow and stress associated with volume expansion are not important. However, a model has been recently proposed in which a pore is formed by perturbation between an oxide layer and an electrolyte. As a result, TiO_2 nanotube arrays using organic solvents have been shown to play an important role in complex formation of pores by ejection of Ti and field-assisted dissolution of oxide layers by F^- ions.

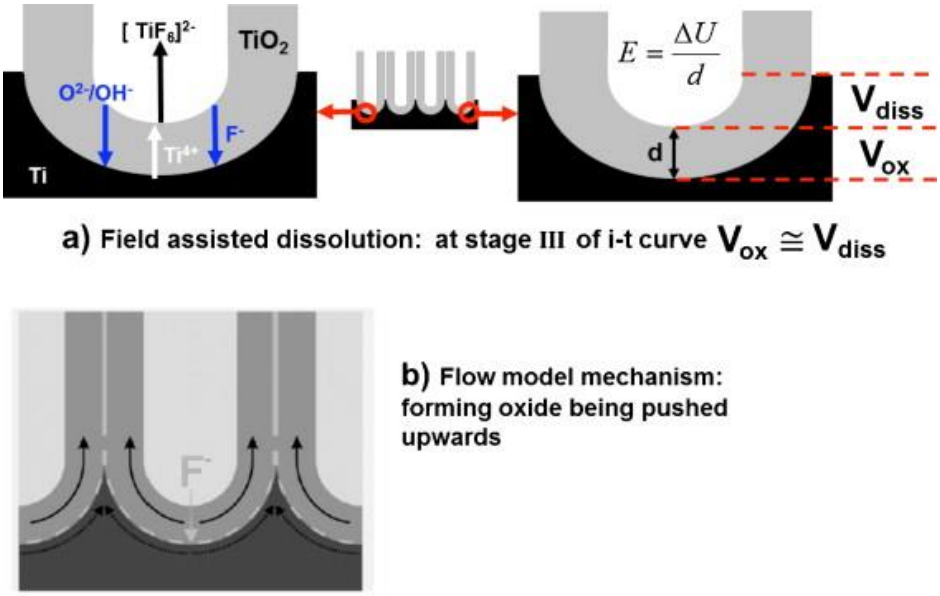

Figure 14. Two representative model of formation of TiO_2 NTAs. [70]

1.2.4 Black TiO_2 and modification of physical properties of TiO_2 NTAs

In general, the anatase phase is known to be the largest electron mobility phase.[91-92] For this reason, applications related to the conduction of electrons such as solar cells[93] and photoelectrochemical cells[94] are related to anatase. However, rutile has an advantage in synthesizing single crystals because rutile is the most thermodynamically stable phase.[95]

In the case of TiO_2 nanotube arrays, both amorphous and anatase phases have a similar band gap of 3.2 eV. Despite similar band gaps, the properties associated with photoelectrochemical reactions such as solar cells are quite different. The electrical conductivity of TiO_2 differs greatly depending on the measurement method, as indicated in the previous review literature.[46] Especially, there is a big difference when measured in a 2 points geometry and 4 points geometry. (**Table 4**) Comparing the results of 4point measurements with bulk, it can be seen that the resistance is smaller in case of nanotube. In addition, electrical conductivity measurements using the impedance method can be explained by the high defect density of anodic TiO_2 nanotubes, which is slower to transport in bulk than transport at grain boundaries. It is also observed that the dependence of temperature on TiO_2 nanotubes is proportional to $T^{-1/4}$, and it is predicted that electrons are transported by Mott variable range hopping conduction mechanism in TiO_2 nanotubes. This implies that the TiO_2 nanotube system is a strongly disordered system with a localized charge-carrier state. (**Figure 15**)

In addition, these TiO_2 nanotubes can be doped in a variety of ways, making it easy to change their conductivity. The overall research trends related to this are summarized in **Figure 16**.[96-97] We used Ar annealing and Ar/H_2 annealing, which are the easiest methods to preserve defects in the TiO_2 nanotube array.

In particular, TiO_2 can produce defects (Ti^{3+} and oxygen vacancies) when subjected to heat treatment in a reducing atmosphere or vacuum, and the color of the TiO_2 varies greatly. Of these, TiO_2 with black color is called black TiO_2. Black TiO_2 was first reported by Chen in 2011 and reported as a photocatalyst with improved optical properties.[98]

TiO_2 NTAs also show a change in the color of TiO_2 when subjected to a heat treatment in a reducing atmosphere or in a vacuum containing hydrogen, and the formula in which the defect is made is as follows.[99]

$$2Ti_{Ti}{}^{X} + O_O{}^{X} \rightarrow 2Ti_{Ti}{}' + \frac{1}{2}O_2 + V_O{}''$$

(Kroger-Vink Notation for crystal defects)

the symbol for the atom involved, or V if the site is vacant;

a superscript indicating the net charge:

- • for charge +1,

- X for zero net charge,

- ′ for charge -1;

As can be seen from the equation, Ti^{4+} ion loses one electron to become Ti^{3+}, and oxygen is converted into oxygen, and the remaining two electrons occupy oxygen vacancy. In the case of hydrogen atmosphere, the following reaction formula is obtained.[100]

$$O_O{}^{2-} + 2Ti^{4+} + H_2 \rightarrow V_O + 2Ti^{3+} + H_2O$$

Hydrogenation is accomplished by the simultaneous formation of O vacancy and Ti^{3+} center.

These oxygen vacancies and Ti^{3+} can be confirmed by various methods. More roughly, it can be confirmed by shift of the XPS spectrum, and more directly by electron paramagnetic resonance (EPR). In addition, we confirmed that it was blue shifted through Raman and confirmed that this is Ti^{3+} center. In the EPR method, the oxygen vacancy is confirmed with high accuracy (g-value = 2) but the Ti^{3+} center is hard to ascertain accurately.[101-102] In addition, we confirm that the charge carrier is increased by the Mott-schottky method or indirectly by the difference of UV-vis spectrum. (**Figure 17**)

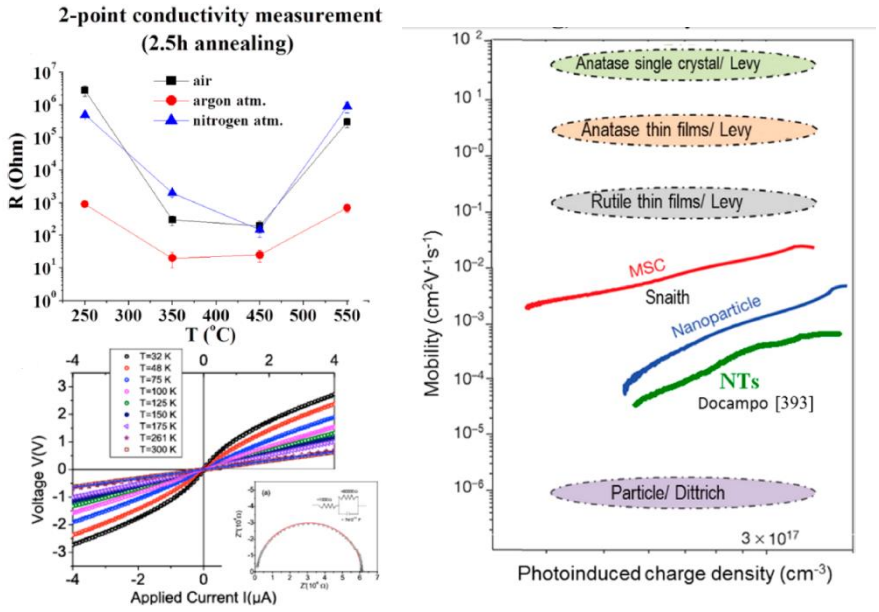

Figure 15. Electrical properties of TiO_2 NTAs. [46]

	TiO_2 NTAs	Polycrystalline bulk anatase	Single crystalline bulk anatase
Resistivity	10^{-2} ohm·cm / 10^{2}~10^{7} ohm·cm*	10^{2}~10^{7} ohm·cm	1.5 ohm·cm
Ref	103-104	105-106	92
	* 2 point measurement		

Table 4 Summary of TiO_2 resistance measurement

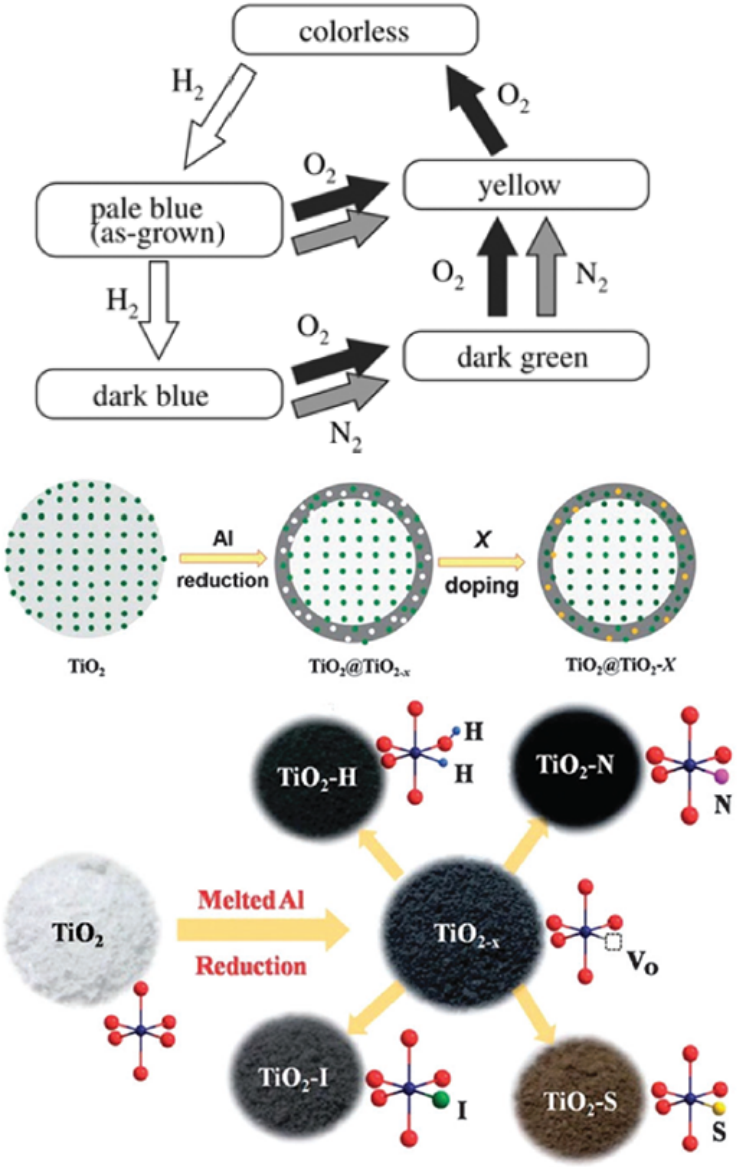

Figure 16. Summary of various doped TiO_2 and its color change characteristics. [96-97]

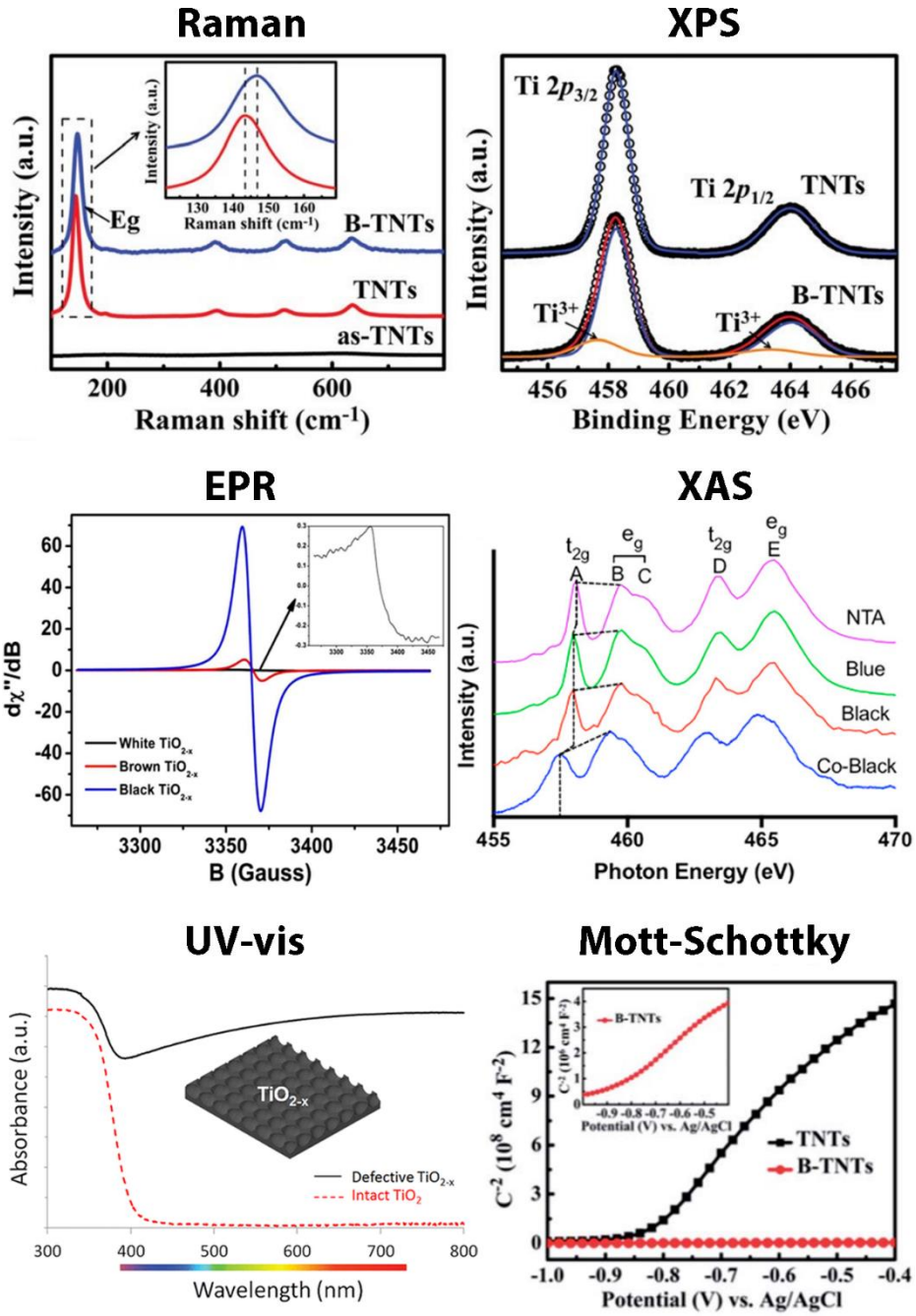

Figure 17. Various methods to identify defect in black TiO_2 NTAs. [101-102]

2. Experimental Details

2.1. Preparation of TiO_2 nanotube arrays (TiO_2 NTAs)

TiO_2 nanotube arrays were synthesized by two-step electrochemical anodization of Ti foil (thickness 0.25 mm, 99.99% trace metals basis (Aldrich)). Before anodization, Ti foils were degreased by sonication in acetone, ethanol and deionized water. The samples were anodized in electrolytes containing Ethylene glycol, 0.25wt% NH_4F and 2.5vol% water. In the first-step anodization, the Ti sheet was anodized at various voltage (30V~70V) for 2hour at room temperature, and then the as-grown TiO_2 nanotube arrays were removed ultrasonically. The same samples underwent the second-step anodization for 30min. After anodization, the samples were cleaned with deionized water and dried under gentle nitrogen stream. Next, the pores of the TiO_2 nanotube arrays were widened by immersing the films in formamide solution containing 0.15M NH_4F and 3.5wt% water at 72℃ for 10min followed by cleaning water. b- TiO_2 was obtained by annealing the samples in H_2(4%)/Ar atmosphere at 450℃ for 1h with a heating rate 5℃/min. c- TiO_2 was obtained by annealing in air at 450℃ for 1h with a heating rate 5℃/min.

2.2. Preparation of the RuO_2@NTAs electrode

Ruthenium oxide nanoparticles were deposited onto NTAs by pulsed electrodeposition (PED). RuO_2 electrodeposition underwent at -1mA/cm^2 in a three-electrode configuration with 50ms on time, and 1s off time using NTAs as the working electrode, Pt wire as the counter electrode, and a saturated calomel electrode (SCE) as a reference electrode. The electrolyte consists of $RuCl_3 \cdot xH_2O$ (10mM) and KCl (0.5M) dissolved in deionized water. After RuO_2 electrodeposition, the fabricated samples were annealed in air at 200℃ for 3h with heating rate 5℃/min.

2.3. Materials Characterization

The morphology of the film was characterized by Field Emission Scanning Electron Microscopy (FE-SEM, JEOL, JSM-7600F) with Energy Dispersive X-ray Spectrometer. X-ray diffraction (XRD) patterns were collected to identify the phase of the fabricated electrode. To investigate the chemical oxidation states of the samples, X-ray photoelectron spectroscopy (XPS, SIGMA PROBE (VG, UK)). To calibrate the binding energy of the samples, C 1s photoelectron peak (284.5eV) was used. The detailed crystallographic structure and morphology is studied by Transmission electron microscopy (JEOL, JEM-2100F).

2.4. Electrochemical measurements

The fabricated electrodes were characterized by cyclic voltammetry (CV) in a three-electrode system consisting of fabricated electrode, Pt wire and saturated calomel electrode (SCE) as working electrode, counter electrode and reference electrode respectively. The schematic view of electrochemical setup is down below. (**Figure 18**)[107] To perform hydrogen evolution reaction (HER) test, the nitrogen purged 0.5M H_2SO_4 electrolyte was used. For chlorine evolution reaction (CER) test, 5M NaCl (pH=2) was employed as electrolyte. The electrical double layer capacitance (EDLC) of electrodes were carried out by using cycling between 0.2V and 0.4V vs RHE at various scan rates of 10mV/s, 25mV/s, 50mV/s, 100mV/s and 200mV/s. The current density at 0.3V vs RHE and the corresponding scan rates were linearly plotted.

The ferrocene ($Fe(C_2H_5)$) solution (2mM) is prepared by dissolving ferrocene in acetone. To reduce the resistance of solution, 0.3M tetrabutylammonium tetrafluoroborate ($[Bu_4N]$ BF_4) is used as supporting electrolyte. For each ferrocene solution, the cyclic voltammetry was recorded in the potential range of $0.6V_{SCE}$ to $1.2V_{SCE}$ at 10mV/s scan rate.

Vanadium redox couple solution is prepared by dissolving 0.1M $VOSO_4$ in 3M sulfuric acid. For each solution, the cyclic voltammetry was conducted in the potential range of $-0.75V_{SCE}$ to $0.75V_{SCE}$ at 50mV/s scan rate.

Electrochemical impedance measurements to obtain the Mott-Schottky plot, using a conventional three-electrode system and a computer-controlled multichannel potentiostat (PARSTAT MC 1000, Princeton Applied Research, USA).

The donor density of b-TiO_2 substrate can be measured through the capacitance measurement. Using Mott-Schottky equation, the carrier density is calculated as follows.

$$\frac{1}{C^2} = \frac{2}{eA^2\varepsilon\varepsilon_0 N_D}\left[(U_S - U_{FB}) - \frac{k_B T}{e}\right]$$

Where C is the space charge capacitance, A is the geometric area of electrode, N_D is the donor carrier density, e is the elementary charge, ε_0 is the permittivity of the free space, ε is the dielectric constant of the electrode material(=48 for anatase TiO_2), U_S is the applied potential, U_{FB} is the flat band potential, k_B is the Boltzmann constant and T is the temperature.

To determine electrochemical characters of interface between electrode and interface, electrochemical impedance spectra (EIS) was measured under various potential from -1V to 2V vs SCE at fix frequency, 1000Hz. When voltage applied electrodes, the electrical capacitance and resistance are defined below. (**Figure 19**) [108] The electrochemical impedance spectroscopy (EIS) is a useful tool for analyzing the electrochemical properties of interfaces. The impedance method is a method of recording a change in capacitance and resistance by applying a small alternating voltage. Electrochemical reactions often occur between the electrodes and the electrolyte, which can be analyzed by the impedance method. When the electrode is negatively charged on a flat electrode, the circuit corresponding to the schematic diagram is as follows. (**Figure 19**)

Also, the impedance value at this time is given by the following equation. [108]

$$Z(\omega) = R_s + \frac{R_p + \sigma\omega^{-\frac{1}{2}}}{\sigma\omega^{\frac{1}{2}}(C_d+1)^2 + \omega^2 {C_d}^2 (R_p + \sigma\omega^{-\frac{1}{2}})^2} + j\frac{\left[\omega C_d \left(R_p + \sigma\omega^{-\frac{1}{2}}\right)^2 + \sigma\omega^{-\frac{1}{2}}\left(C_d\sigma\omega^{\frac{1}{2}} + 1\right)\right]}{(C_d\sigma\omega^{\frac{1}{2}}+1)^2 + \omega^2 {C_d}^2 (R_p + \sigma\omega^{-\frac{1}{2}})^2}$$

Here, $\omega = 2\pi f$, f is frequnecy, $j = \sqrt{-1}$, and

$$\sigma = \frac{RT}{\sqrt{2}n^2F^2A}\left(\frac{1}{D_O^{\frac{1}{2}}C_O(x,t)} + \frac{1}{D_R^{\frac{1}{2}}C_R(x,t)}\right)$$

where *A* is the electrode area, *C*s are concentrations of subscripted species at a distance *x* from the

electrode surface, and *t* is time

When the frequency goes to infinity, the following equation can be used.

$$Z(\omega) = R_s + \frac{R_p}{1+\omega^2 {C_d}^2 {R_p}^2} - j\frac{\omega C_d {R_p}^2}{1+\omega^2 {C_d}^2 {R_p}^2} = Z'(\omega) - jZ''(\omega)$$

Conversely, when the frequency converges to 0, it becomes simpler as follows.

$$Z(\omega) = R_s + R_p + \sigma\omega^{-\frac{1}{2}} - j(\sigma\omega^{-\frac{1}{2}} + 2\sigma^2 C_d) = Z'(\omega) - jZ''(\omega)$$

The nyquist plot shows the real part on the x axis and the imaginary part on the y axis. In general, it can be confirmed that a semicircle is formed at a high frequency and a linear shape is formed at a low frequency. In this case, it is possible to derive a different graph depending on the ratio of the electron transfer rate to the diffusion rate. (**Figure 20**) [108]

In TiO_2 nanotube arrays, two types of models are commonly used. (**Figure 21**) [109-110] Recently, the second model is successful because in most cases wall is very conductive due to its thin thickness(~10nm). So we selected the second model to investigate TiO_2 nanotube array interface.

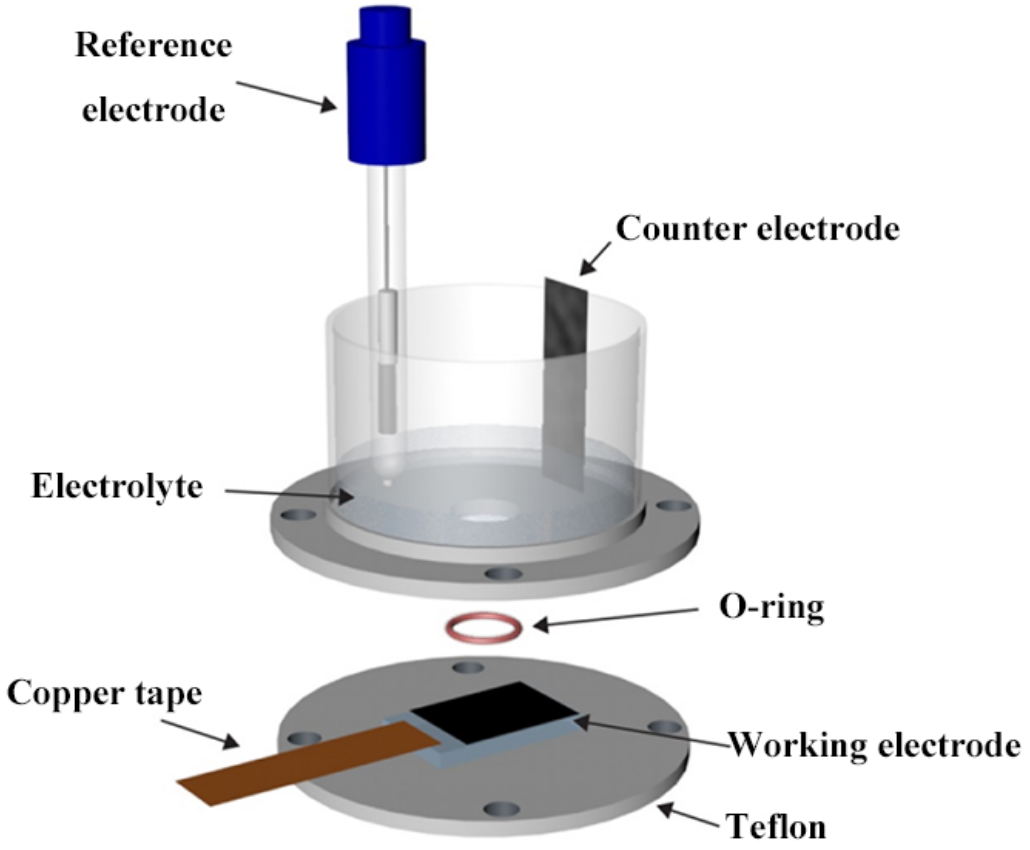

Figure 18. Schematic view of 3-electrode system used in our study. [107] This system is also applied in fabrication of anodized TiO_2.

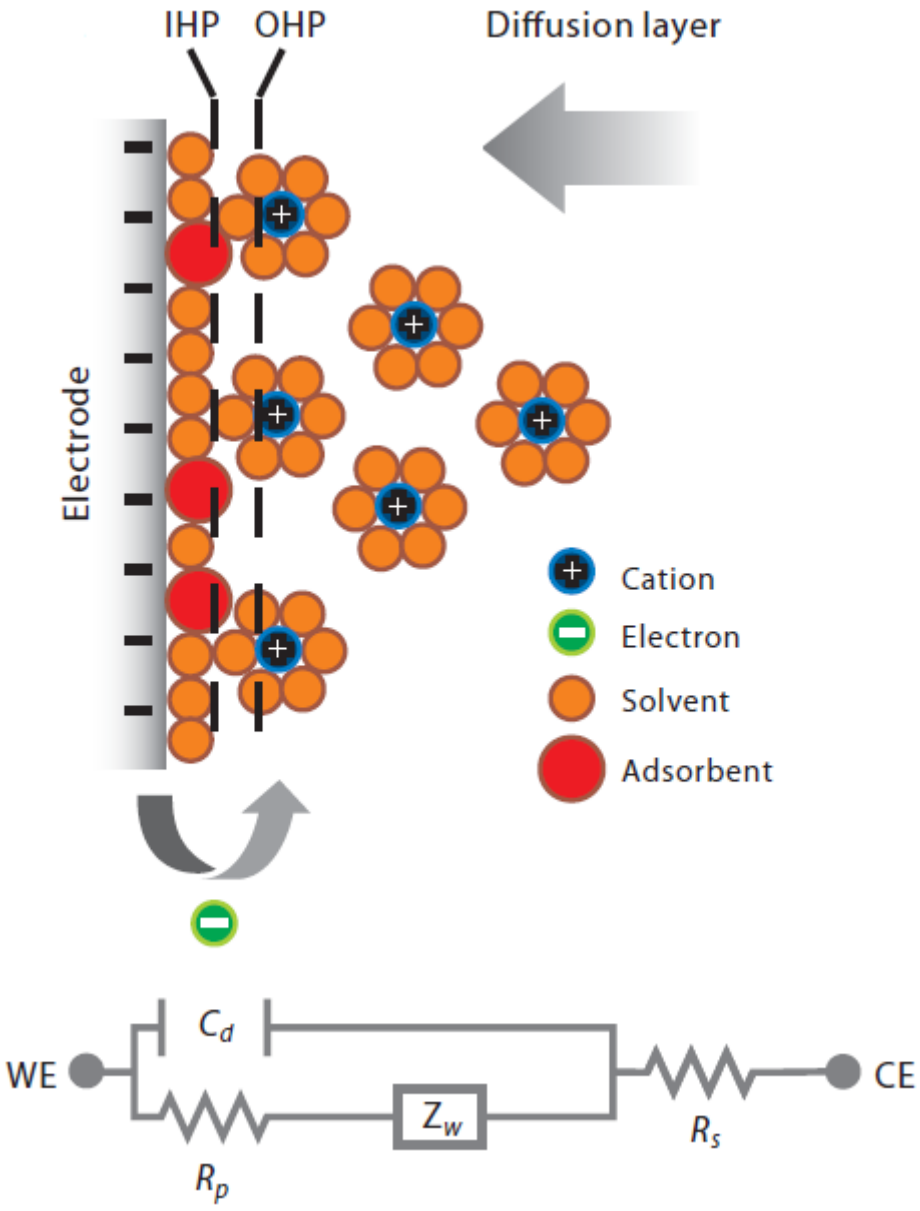

Figure 19. General schematic view of electrolyte and electrode interface. [108]

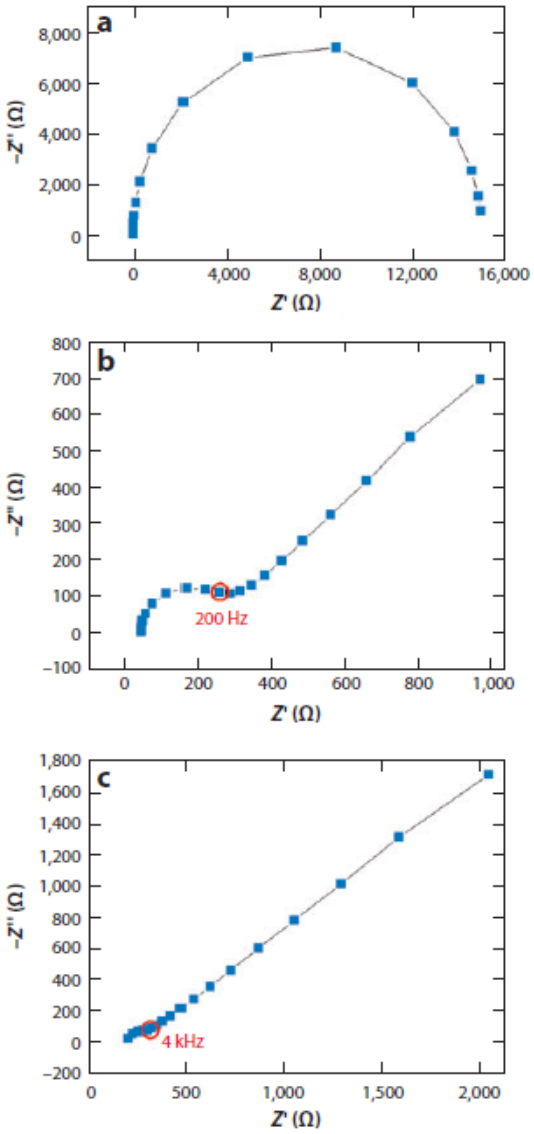

Figure 20. Three typical cases of electrochemical impedance spectroscopy (a) fast diffusion rate compared to electron transfer rate, (b) similar diffusion compared to electron transfer rate, (c) slow diffusion compared to electron transfer rate. [108]

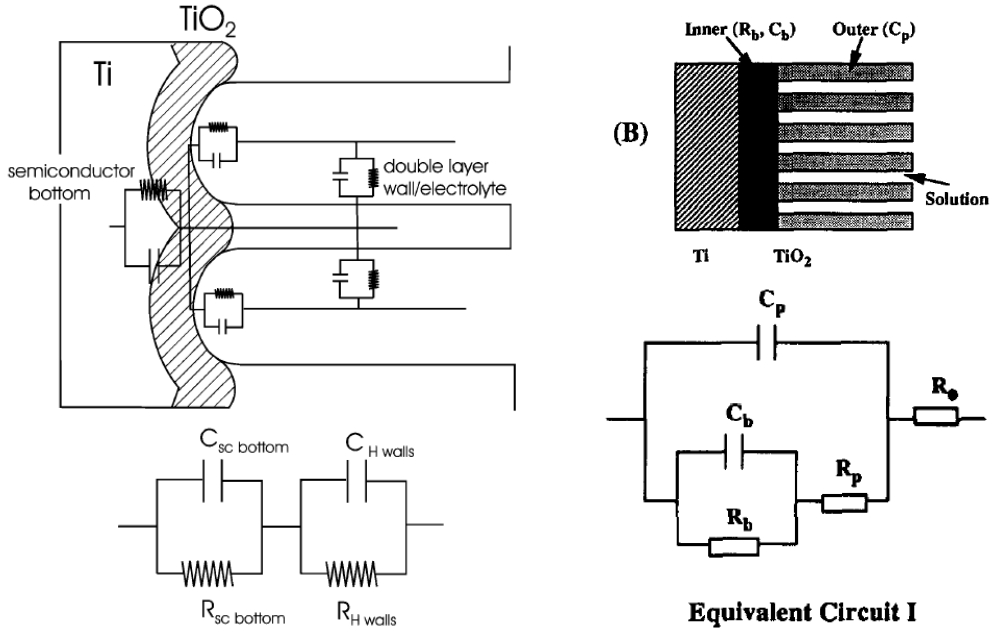

Figure 21. Two typical cases of model of TiO_2 nanotube arrays. [109-110]

3. Results and discussion

3.1 Preparation of TiO_2 NTAs

3.1.1 voltage dependence of TiO_2 NTAs

First, the current profile seen in typical TiO_2 nanotube array formation is as follows. As shown in the **Figure 22**, the current decreases dramatically as TiO_2 is formed, and steady state is reached at some moment and a constant current is maintained. At this time, it is known that the rate of formation and dissolution of oxide is the same.[111] The reason for the dullness in the graph is that chemical dissolution does not occur constantly when initial pore is generated. When 2nd anodization is performed, we can obtain a graph similar to the typical anodization process.

The magnitude of the diameter produced by varying the applied voltage was investigated with the same electrolyte conditions. TiO_2 nanotubes are known to increase in diameter as the voltage increases. This is because the electric field affects the migration of ions as they increase and affects the diameter. As the voltage increases, the electric field also increases and the higher electric field weakens the Ti-O bond and promotes chemical dissolution by the F-ion. This creates a dimple of larger diameter, which increases the outer diameter. (**Figure 23**) In addition, as the applied voltage increases, the wall thickness also increases, which can be explained by the increase in the thickness of the barrier oxide.

In addition, it can be seen that the length of the TiO_2 nanotubes linearly increases as the applied time becomes longer. (**Figure 24**)

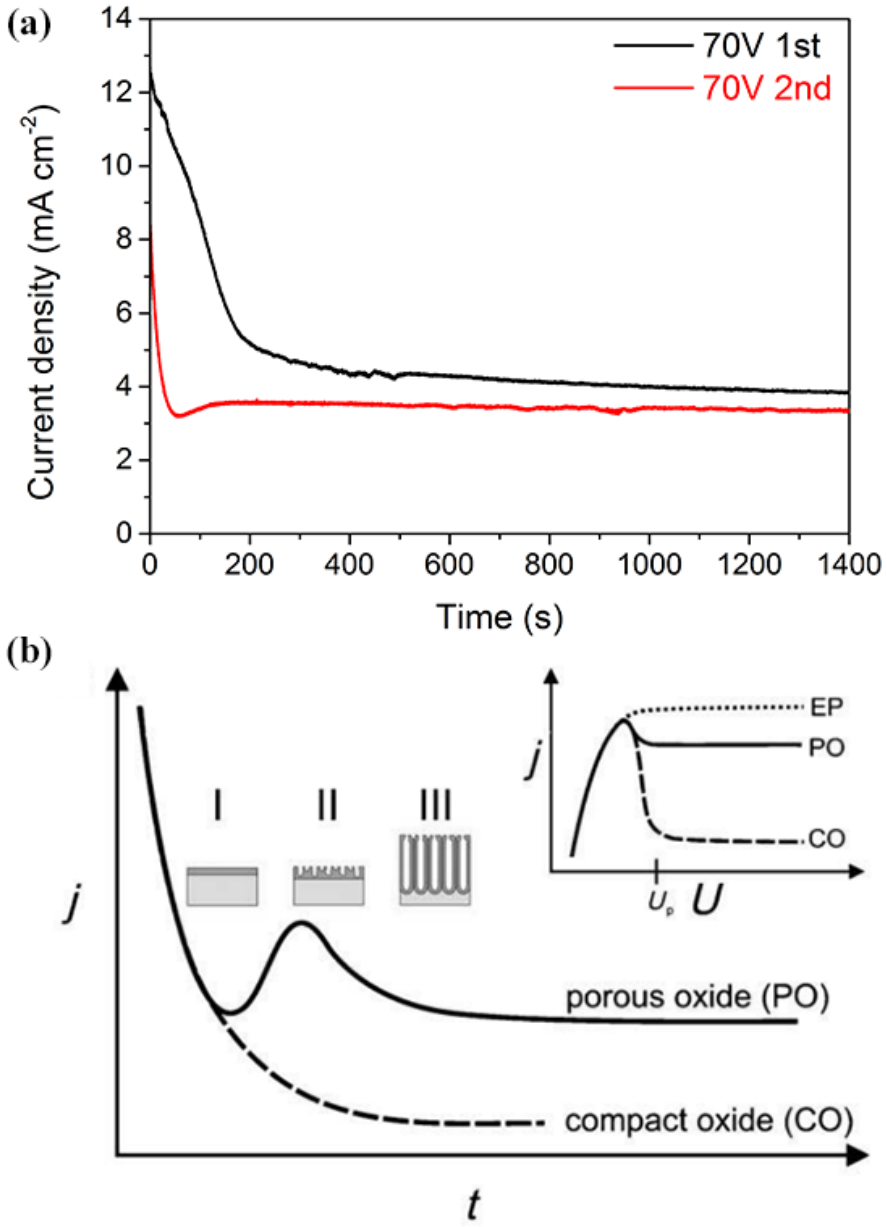

Figure 22. (a) Obtained current profile characteristics and (b) typical current-time characteristics.[111]

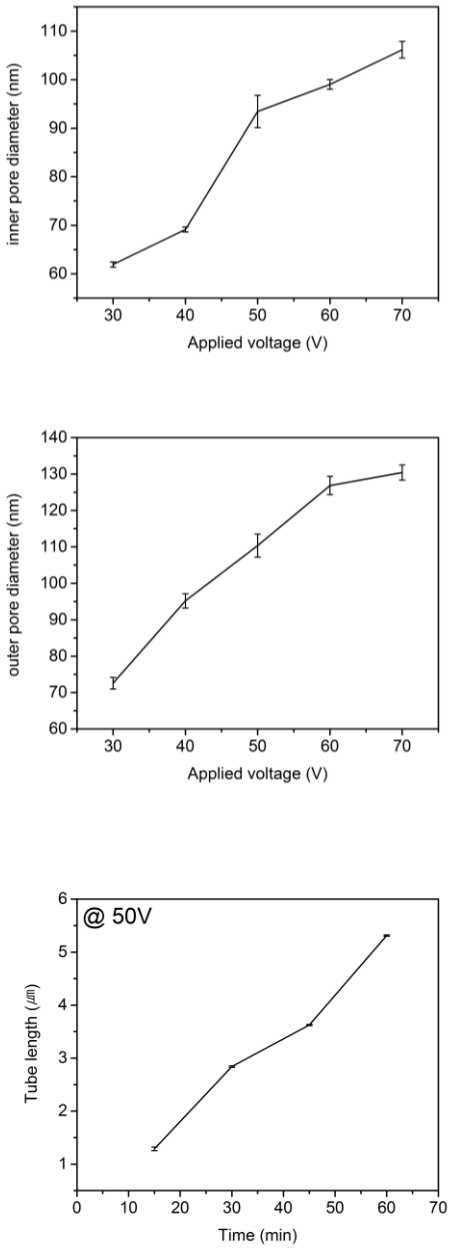

Figure 23. Voltage dependence of pore diameter(inner/outer), Time dependence of tube length

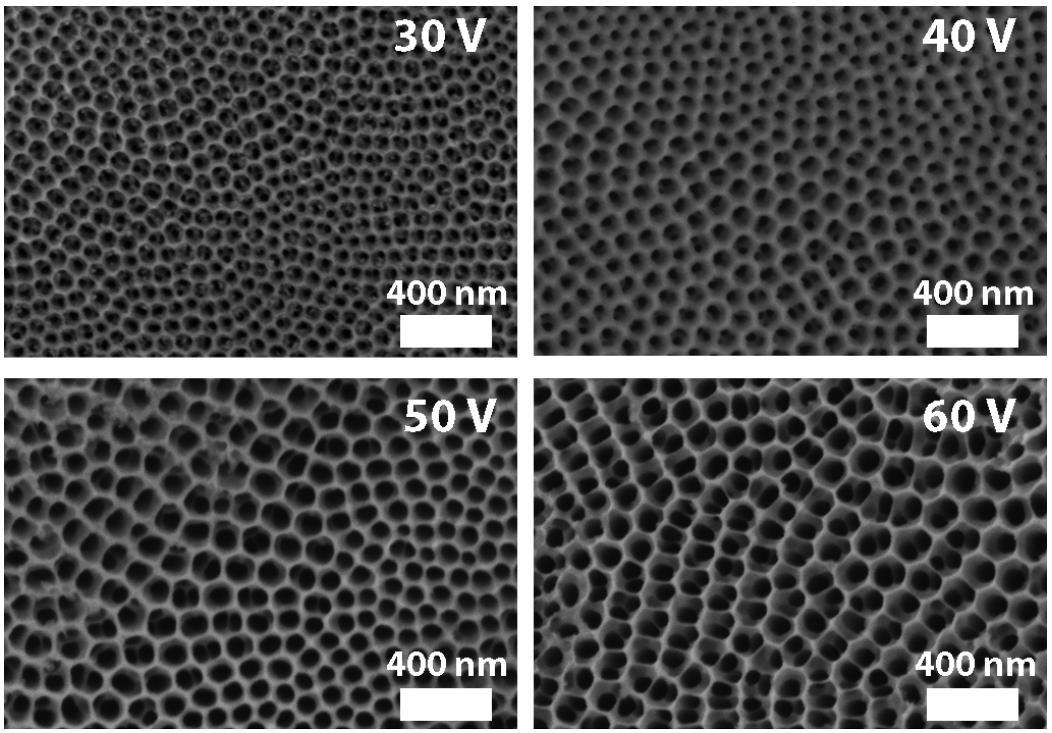

Figure 24. Comparison of samples which is made under different voltages

3.1.2 effect of pore widening

The TiO_2 nanotube array can be chemically treated to enlarge the bore and eliminate the tube wall. This is called the pore widening process and is generally performed in a solution containing F- ions. Because F-ions are known to dissolve TiO_2 even during the anodization process, a solution containing F-ions can dissolve some of the TiO_2 nanotube arrays made. During the pore widening process, the length of the nanotubes decreases slightly and the thickness of the tube wall decreases. It is clearly shown in SEM images. (**Figure 25**)

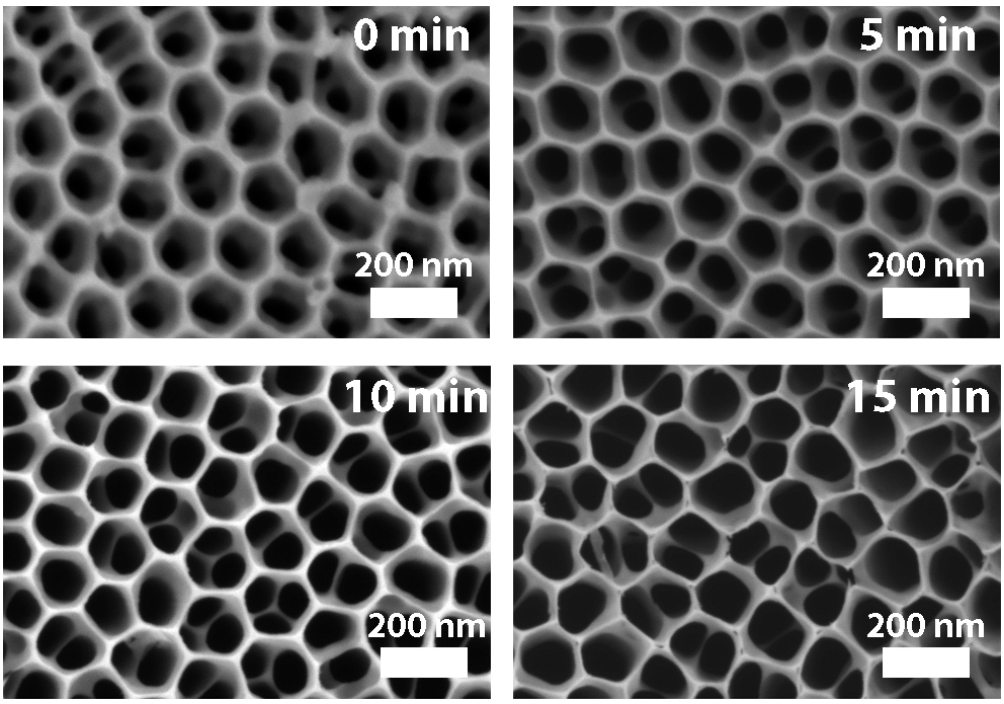

Figure 25. Comparison of samples which is different in pore widening time.

3.2 Preparation of TiO_2@RuO_2 electrodes

3.2.1 pulse electrodeposition and constant current electrodeposition

In the TiO_2 nanotube array, electrodeposition method was used to load the catalyst. The electrochemical reactions for depositing RuO_2 through electrodeposition are as follows.[112-113]

Cathode: $O_2 + 2H_2O + 4e^- \rightarrow 4OH^-,\ 2H_2O + 2e^- \rightarrow H_2 + 2OH^-$

$Ru^{3+} + OH^- \rightarrow RuO_x(OH)_y \rightarrow RuO_2$

Competing reactions: $Ru^{4+} + 4e^- \rightarrow Ru$

An OH^- generating reaction takes place near the cathode, where Ru^{3+} meets Ru-based hydroxide. RuO_2 may be formed when the oxidation proceeds a little more. Cathodic pulses give Ru^{4+} reduction to Ru. According to the pourbaix diagram (**Figure 26**) [114], the lower the pH, the more stable the Ru metal, and the higher the pH, the more thermodynamically stable oxyhydroxide. Our $RuCl_3$ precursor can effectively inhibit the deposition of Ru metal due to its high pH. In addition, even when Ru metal is deposited, it can be confirmed that RuO_2 is sufficiently converted through the heat treatment process.

Typical methods of electrodeposition include constant current deposition and constant voltage deposition. In the case of deposition at a constant voltage, since the

thermodynamic potential is controlled, the desired reaction can be promoted. However, it is difficult to precisely control how much charge contributes to deposition. We experimented with a constant current to control the amount of loading RuO_2 loading.

In the case of deposition by a general constant current method, it can be observed that the deposition does not proceed well because the electrolyte does not enter the nanotube structure well. However, when the deposition is performed by the pulse method, it is easy to observe the deposition of the electrolyte into the nanotube and the deposition of RuO_2 in the nanotube by SEM or TEM. (**Figure 27**)

This process can be illustrated as follows. (**Figure 28**) In the case of pulse electrodeposition with a well-diffused electrolyte, the reaction to RuO_2 occurs well, whereas in the case of a constant current method in which the electrolyte does not diffuse for a long time, RuO_2 grows only on the top of the nanotube. This makes it impossible to use the advantage of enlarging the specific surface area, and the characteristics also deteriorate.

The model describing pulse electrodeposition is as follows. Often, using the pulse method has two advantages: First, it removes the electrical double layer around the cathode, allowing the electrolyte to transfer to the nanostructure. Second, if the current is very high, it may allow time for ions to diffuse well into the depletion region near the electrode. For this reason, electrodeposition is performed using a pulse. Eventually, the pulse duration (T_{on}) should be less than the time at which the concentration of the reactants at the interface is zero (τ), and be much longer than the time to fill the electrical double

layer (EDL) capacitance (T_c), which is prerequisite to occur faradaic reaction. Also, the time to turn off the pulse (T_{off}) should allow enough time to discharge the electrical double layer (T_d). These conditions can be written as follows.

$$T_c < T_{on} < \tau$$

$$T_{off} >> T_d$$

Where T_c is the EDL charging time, T_d is the discharging time, and τ is the migration time, which means the time it takes for the interfacial concentration to drop to zero. These values are given by the following formula.[115-116]

$$T_c = \frac{17}{J_p}$$

$$T_d = \frac{120}{J_p}$$

$$\tau = \frac{\pi D {C_0}^2 (nF)^2}{4{J_p}^2}$$

Where J_p is peak current density of pulse (unit : A/m^2), and the unit of T_c and T_d is μs. D is diffusion coefficient of metallic ion, which have a value about 10^{-6} cm^2/s. C_0 is the bulk concentration of the given ions (mol/L), n is the number of electron engaged in electrodeposition, F is Faraday's number (96486C/mol). When we put the relevant parameters (J_p=10A/m^2 = 1mA/cm^2 10mM Ru^{3+} ion), in our experiment) into the equation related to the formation of RuO_2 leads to the following parameters:

$$T_c = 1.7\mu s, T_d = 12\mu s, \tau = \ 2.92s$$

Therefore, we select the T_{on} as 50ms, T_{off} as 1s respectively.

The voltage profile of pulse electrodeposition is as shown below (**Figure 29**). As shown in transient voltage profile, the hydrogen evolution is not detected, which indicates no mass transfer limit during electrodeposition. If hydrogen evolution or other side reaction occurs, the voltage profile changes. (**Figure 30**) [117]

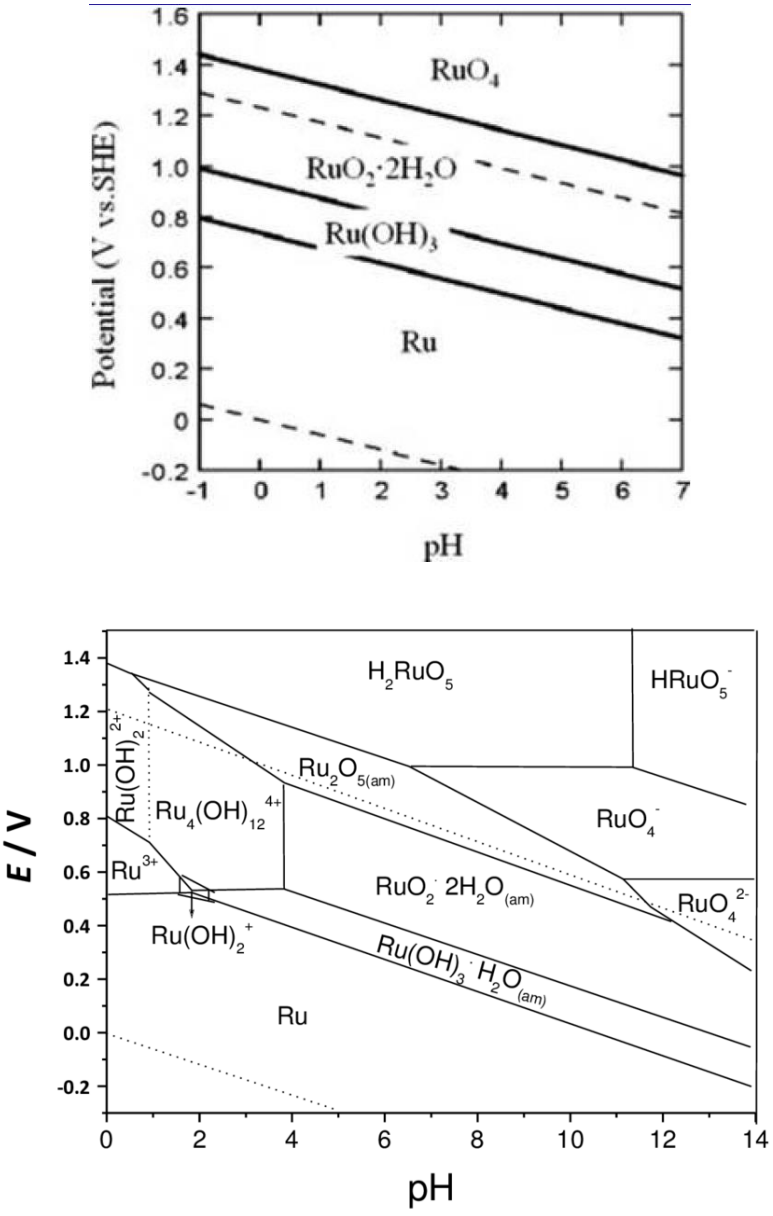

Figure 26. Pourbaix diagram of Ru-H_2O system. This graph indicates thermodynamically stable phases at a given voltage and pH. [114]

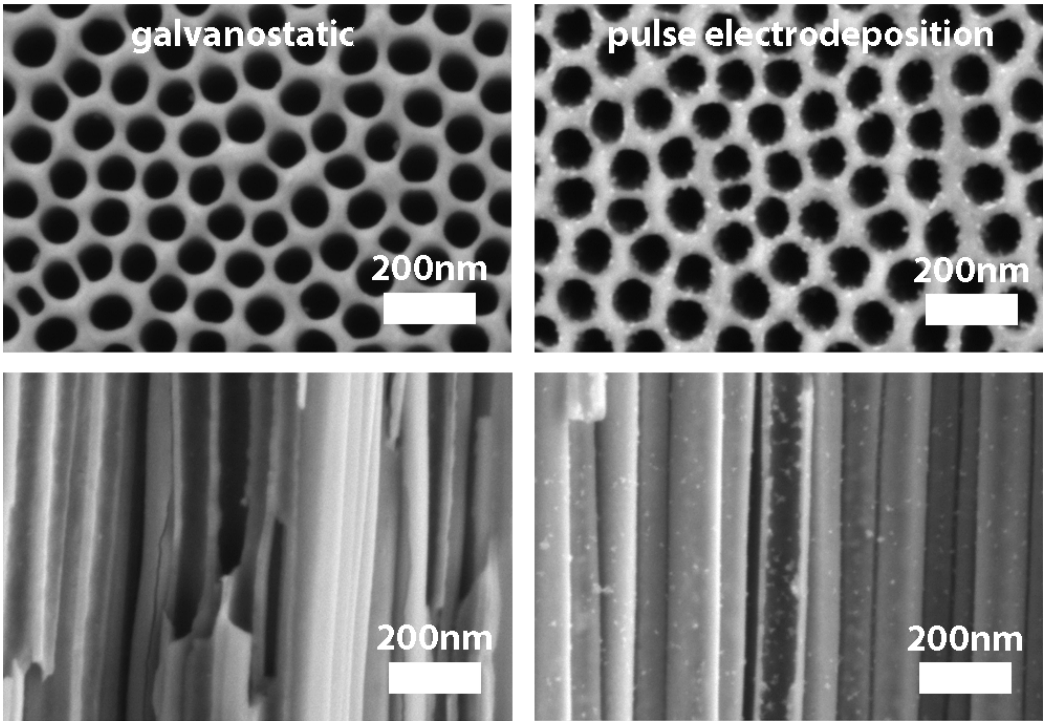

Figure 27. Comparison of TiO_2@RuO_2 electrodes which is fabricated by constant-current method and pulse electrodeposition.

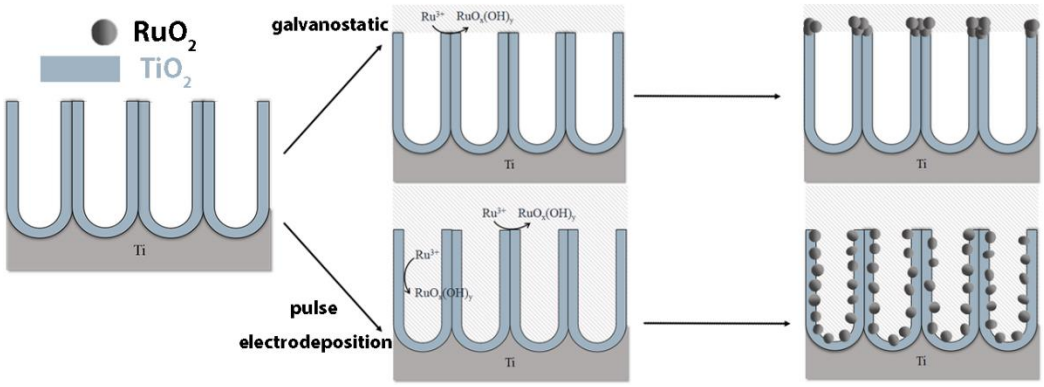

Figure 28. Schematic view of pulse electrodeposition and galvanostatic electrodeposition.

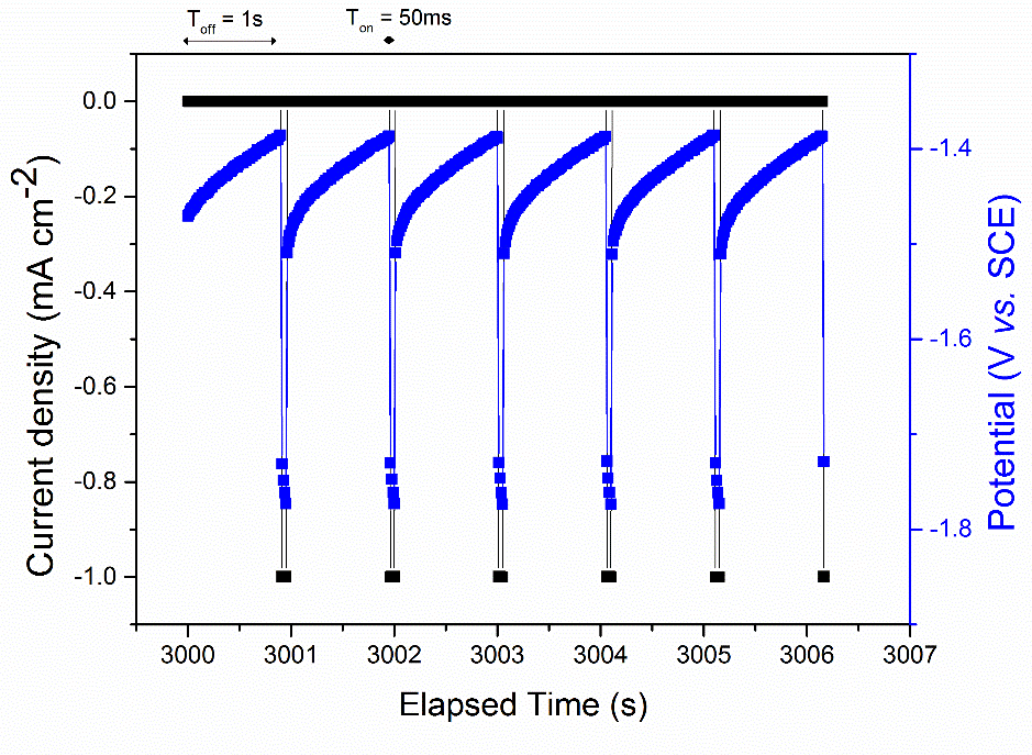

Figure 29. Potential transients during pulse electrodeposition.

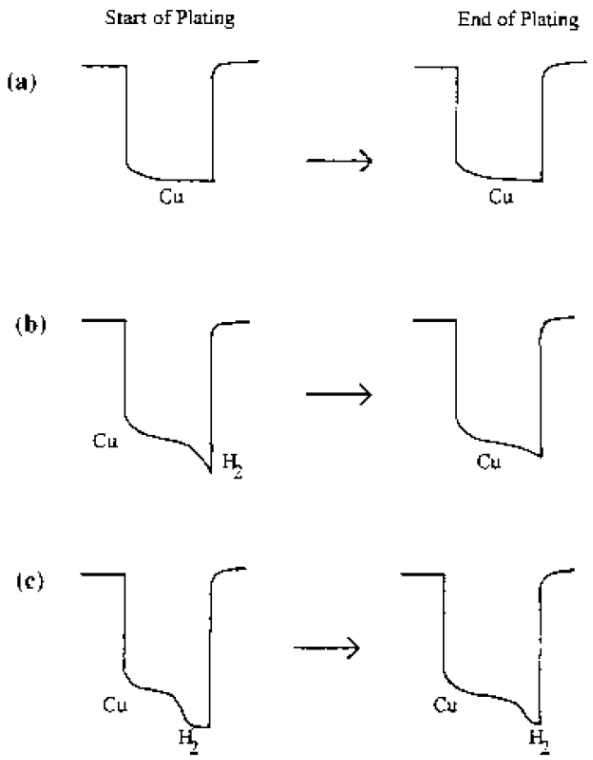

Figure 30. Potential transients during different condition of pulse electrodeposition. (a) no mass transfer limit (b) non steady-state (transient) mass transfer limit (c) steady-state mass transfer limit. [117]

3.2.2 effect of annealing condition

TiO_2 nanotube arrays tend to change their electrical properties according to the heat treatment conditions. When RuO_2 is deposited on a TiO_2 nanotube array, the electrodeposition configuration may also change. However, as the nanotube arrays were annealed, the shape of the deposition did not change significantly. (**Figure 31**) This is because the cathodic pulse is used for deposition. TiO_2 nanotube arrays vary in their properties depending on the heat treatment conditions, but they are not significantly different in anodic and cathodic environments. As evidence for this, Vanadium redox couple cyclic voltammetry was confirmed. (**Figure 39a**) As it is shown here, the current flowing in the reduction potential does not change much. Other studies also show that there is no significant difference in conductivity at the reductive potential.[118]

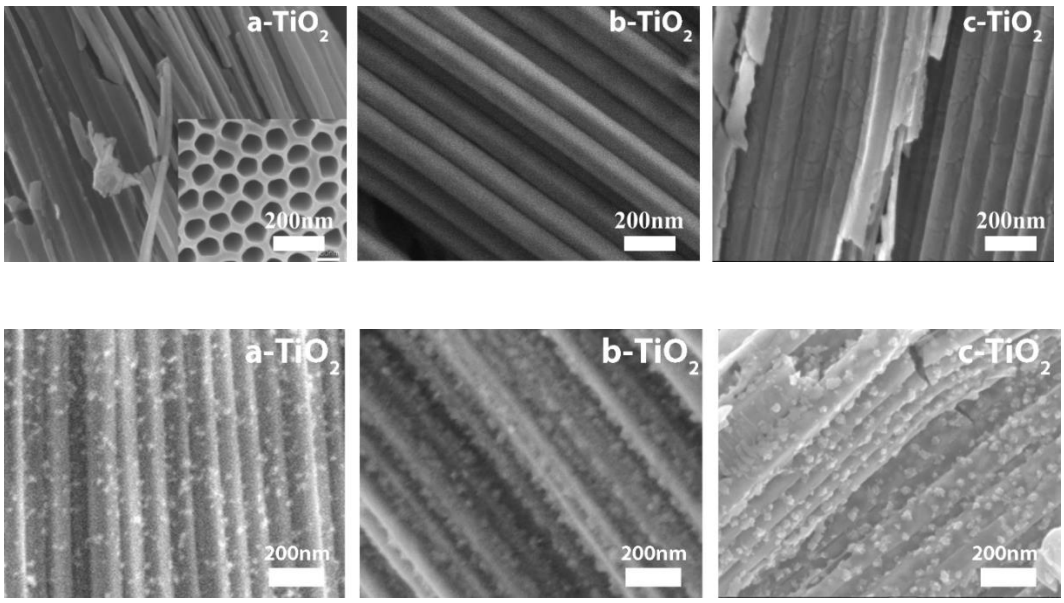

Figure 31. Morphology of TiO_2@RuO_2 electrodes which fabricated under different heat treatment.

3.3 Characterization of TiO_2@RuO_2 electrodes

3.3.1 Materials characterization

Figure 32a show the X-ray diffraction (XRD) patterns of the bare- and RuO_2-loaded TiO_2 NTAs with various annealing conditions. The amorphous as-anodized NTAs (a-TiO_2; amorphous TiO_2) crystallize to the anatase phase after annealing (c-TiO_2; crystalline TiO_2), which is consistent with the literatures. It has been reported that the anatase-to-rutile phase transformation can be facilitated under the reducing atmosphere. However, in our study, the NTAs annealed under the reducing atmosphere (b-TiO_2; black TiO_2) still maintain the anatase phase, while their color change to black (inset of Fig. 26a). This observation indicates that the annealing condition is enough for the crystallization of the anatase phase and for generating a significant amount of defects (or color centers) in the lattice of anatase crystals, but not enough for the anatase-to-rutile phase transformation. It should be noted that no peaks from the RuO_2 crystals can be observed from the XRD patterns of RuO_2-loaded TiO_2 NTAs. However, the existence of the RuO_2 can be confirmed by the X-ray photoelectron spectroscopy (XPS) shown in **Figure 32b, c**. **Figure 32b** exhibits a typical Ru 3d spectrum of the RuO_2, where a peak associated with RuO_2 (280.37eV, 284.54eV), shake-up feature (i.e., Ru3d peak at 282.35eV, 286.55eV), and RuOH (283.3eV).[119-121] Also, C 1s (284.5eV and 297.4eV) is observed due to carbon contamination of the samples. **Figure 32c** also shows a typical O 1s spectrum of RuO_2, where the peak at 529.1 eV is assigned to lattice oxygen in RuO_2. Other peaks at 530eV

and 531.1eV are associated with OH and H_2O, respectively.[122] Due to water affinity of RuO_2, chemisorbed atomic oxygen can be observed. Therefore, it can be concluded that the RuO_2 has deposited successfully on the TiO_2 NTA electrode.

Additionally, the O 1s spectra of b-TIO_2 and c-TiO_2 compared in **Figure 33a**. It can be seen that c-TiO_2 is shifted toward high binding energy compared to b-TiO_2 indicating the density of the electron is reduced. This results can be associated with decrease of oxygen vacancy in c-TiO_2. When RuO_2 is deposited onto TiO_2 nanotube arrays, the peak at 462.2eV due to ruthenium oxide can be observed. This is the result which confirms the deposition of RuO_2. **Figure 33b** shows Ti 2p spectra of b-TiO_2 and c-TiO_2. Ti 2p spectra also shows that c-TiO_2 is shifted toward high binding energy as compared to b-TiO_2. This may also be related to the presence of Ti^{3+} defects in b-TiO_2.

Figure 34 displays the electron microscopy images of the bare- and RuO_2-loaded TiO_2 NTAs. The vertically aligned as-anodized TiO_2 NTAs (a-TiO_2) with an average pore diameter of 100 nm and an average tube length of 4 μm can be prepared after the anodization process (**Figure 34a**), and their morphology does not change significantly after annealing regardless of the atmosphere (**Figure 34b, c**). It can be confirmed from the SEM images (**Figure 34d**) that the nano-sized RuO_2 catalysts are successfully deposited on the TiO_2 NTAs, which is consistent with the XPS analysis (**Figure 34b, c**). It is obvious from **Figure 34e, f** that the density and size of the RuO_2 nanoparticles increases with increasing number of deposition cycles (*i.e.* longer deposition), and thus the amount of RuO_2 catalysts loaded on the TiO_2 NTAs also increases. In addition to the

SEM analysis, the TEM/EDS analysis (**Figure 34g, h**) reveals that the RuO_2 catalysts are uniformly deposited on the surface of the TiO_2 NTAs.

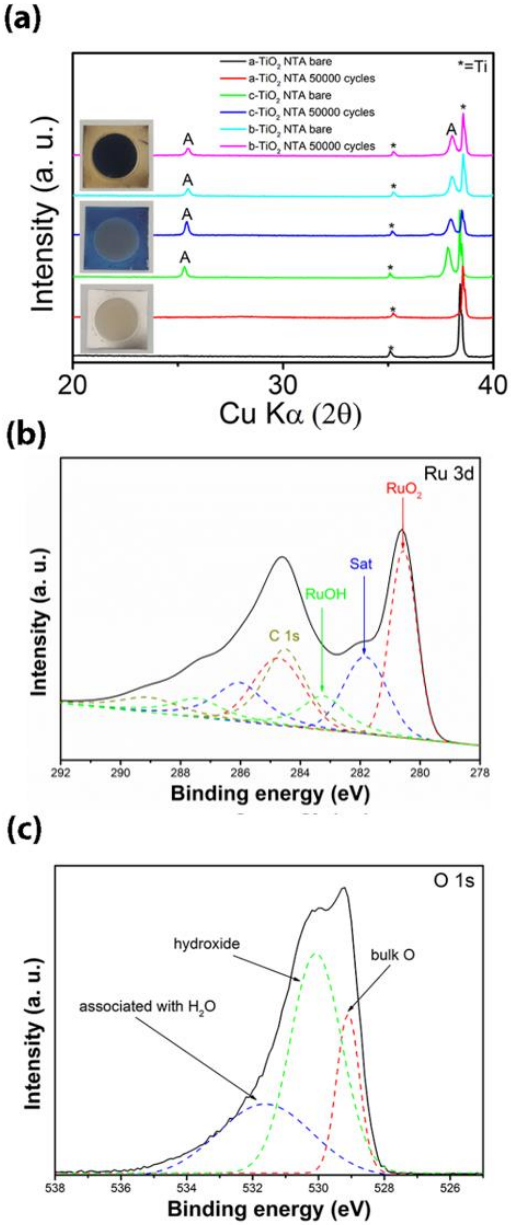

Figure 32. (a) XRD spectra of c-TiO_2 NTAs, different loading of RuO_2 (insets: optical image of a-TiO_2, c-TiO_2, b-TiO_2 NTAs) (b) XPS Ru 3d spectra of c-TiO_2@RuO_2 50000 pulse cycles (c) XPS O 1s spectra of c-TiO_2@RuO_2 50000 pulse cycles.

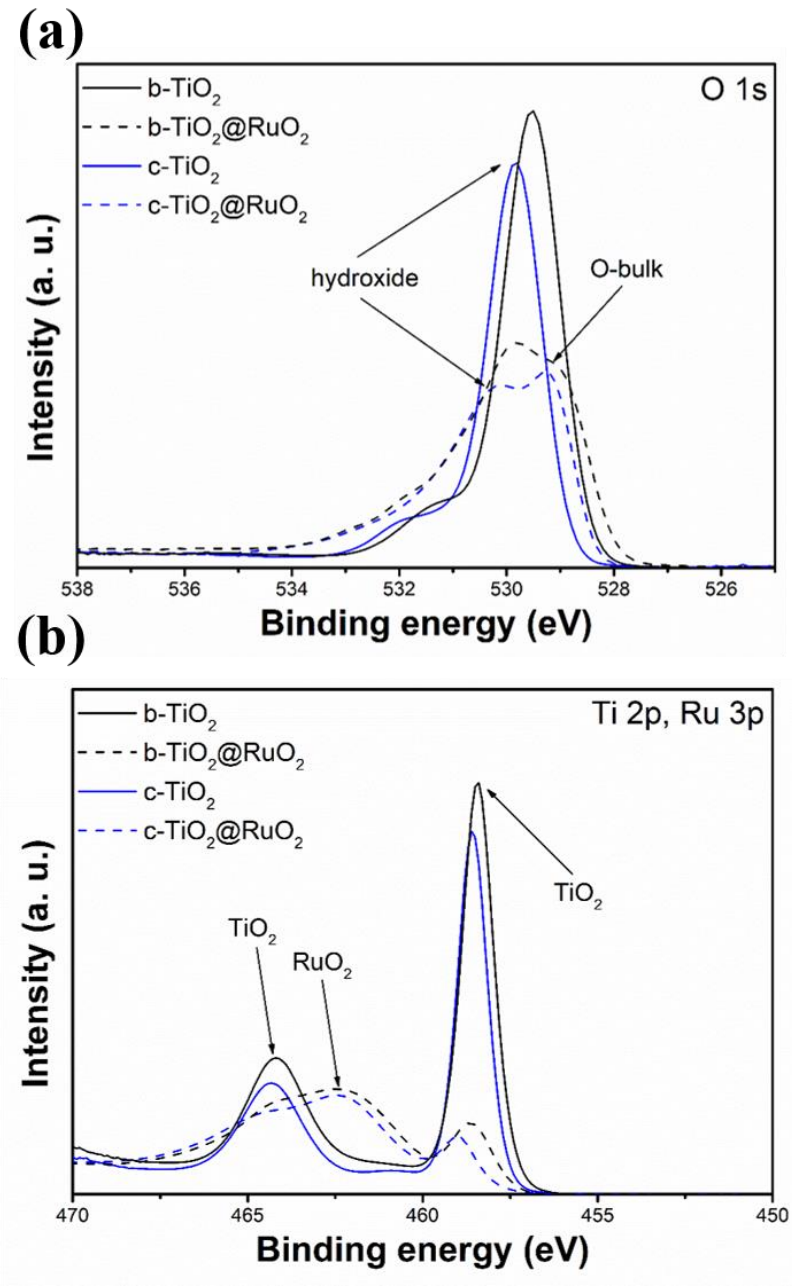

Figure 33. Comparison of (a) XPS O 1s spectra of b-TiO_2 and c-TiO_2, (b) XPS Ti 2p spectra of b-TiO_2 and c-TiO_2

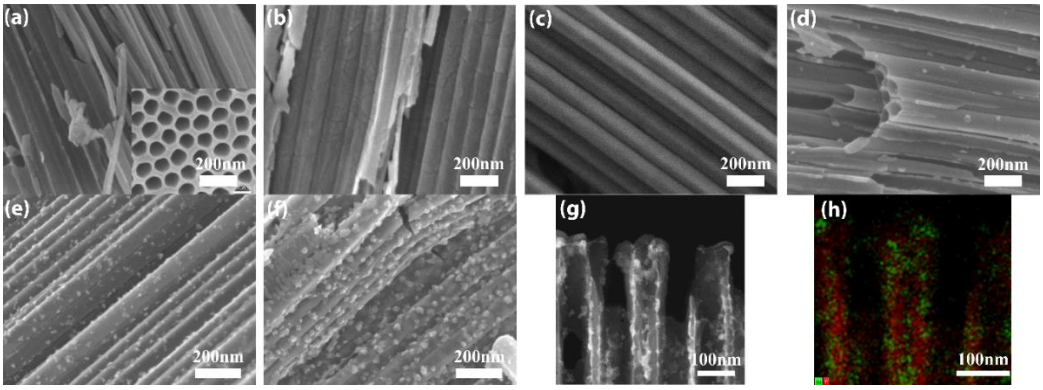

Figure 34. SEM image of (a) a-TiO_2@ RuO_2 10000 pulse cycles (inset: top view of the same sample) (b) a-TiO_2@ RuO_2 30000 pulse cycles (c) a-TiO_2@ RuO_2 50000 pulse cycles (d) c-TiO_2@ RuO_2 50000 pulse cycles (e) c-TiO_2@ RuO_2 50000 pulse cycles (f) a-TiO_2@ RuO_2 50000 pulse cycles. TEM image of (g) c-TiO_2@ RuO_2 50000 pulse cycles (h) EDS mapping of selected area.

3.3.2 Electrochemical analysis

3.3.2.1 Evaluation of catalytic activity

Figure 35 compares the electrocatalytic properties of the RuO_2-loaded TiO_2 NTAs. Bare TiO_2 NTAs without RuO_2 catalysts do not show electrocatalytic activity regardless of the annealing condition. The chlorine evolution reaction (CER) activity of RuO_2-loaded a-TiO_2 NTAs (Fig. 28a) increases with increasing amount of RuO_2 loading. The overpotential of current density at 10mA/cm2 is 134mV, 160mV, 233mV in order of decreasing loading content. This is due to the increase of the electrochemical surface area. In spite of the reasonable CER activity, the a-TiO_2 NTAs are not stable during the electrochemical reaction (**Figure 36**). Although the c-TiO_2 NTA arrays and b-TiO_2 NTAs arrays exhibit better stability than the amorphous counterpart (**Figure 36**), the RuO_2-loaded c-TiO_2 NTAs do not show the CER activity at all (**Figure 35b**). This is a somewhat unexpected result, because the same electrode shows reasonable catalytic activity when used for HER (**Figure 35c**). Given that the charge transfer or the redox reaction at the RuO_2/electrolyte interface is good enough, it is likely that the conductivity of the supporting electrode (*i.e.* c-TiO_2 NTAs) results in the poor CER activity. This hypothesis makes sense, because the anatase TiO_2 is known to exhibit much higher electrical conductivity under cathodic potentials (*e.g.* HER) than anodic potentials (*e.g.* CER).[118] In the same context, the b-TiO_2 NTAs can be a good candidate for both of CER and HER,

because they are crystalline (anatase phase) and the reduced TiO_2 generally shows higher conductivity than the stoichiometric counterparts.[104] The carrier concentration of the b-TiO_2 NTAs determined from the capacitance measurement (*i.e.* Mott-Schottky plot) is higher than the c-TiO_2 NTAs by 5 orders-of-magnitude, indicating that the b-TiO_2 is a degenerated semiconductor with high conductivity (**Figure 37**). Also, its value is well consistent in the literature.[123] Although nanostructures exaggerate donor density because of its high electrochemical surface area,[101] in case which has similar nanostructures, it is possible to compare the relative amounts. As shown in **Figure 37**, the slopes of the graph are positive, indicating that annealed TiO_2 NTAs are n-type semiconductors. This result matches well compared to other literature.[124] In case of b-TiO_2, the charge density was drastically increased compared with c-TiO_2. This may be explained the non-stoichiometry nature of as-grown TiO_2 NTAs. As previous paper demonstrated[125], the as-grown TiO_2 NTAs have high number of defects, therefore after Ar-annealed, the defective nature is preserved. This may be attributed to high donor density of b-TiO_2.

Figure 38 compares the HER and CER activities of c-TiO_2 NTAs and b-TiO_2 NTAs in the presence of the RuO_2 catalyst. As can be expected from the CV curves, both of them show reasonable HER activity. Interestingly, the RuO_2-loaded b-TiO_2 NTAs exhibit a good CER activity if the amount of the catalyst is good enough (i.e. 50000 cycles). The overpotentials of the current density 10 mA/cm^2 and 100 mA/cm^2 are 130mV and 425mV, respectively, which is comparable to the reported values of RuO_2-based CER catalysts (**Table 5, Figure 39**). Therefore, it can be concluded that the b-TiO_2 NTAs are

very promising scaffold and supporting electrode for loading electrocatalysts especially working under universal potentials like CER and HER. (summarized in **Table 6**)

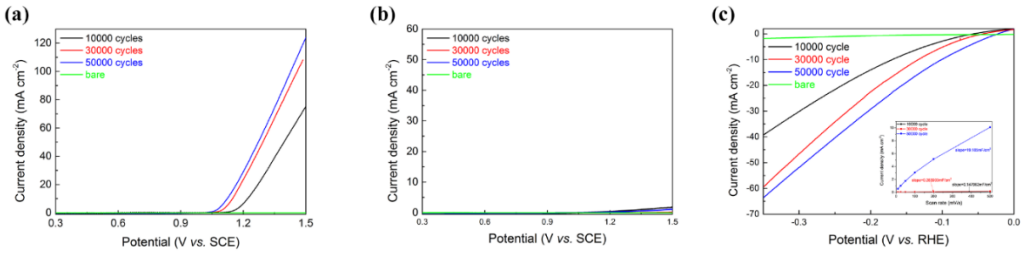

Figure 35. Monitoring CER activity of a) a-TiO_2@RuO_2 NTAs b) c-TiO_2@RuO_2 NTAs and HER activity of c) c-TiO_2@RuO_2 NTAs (insets: electrochemical surface area measurement)

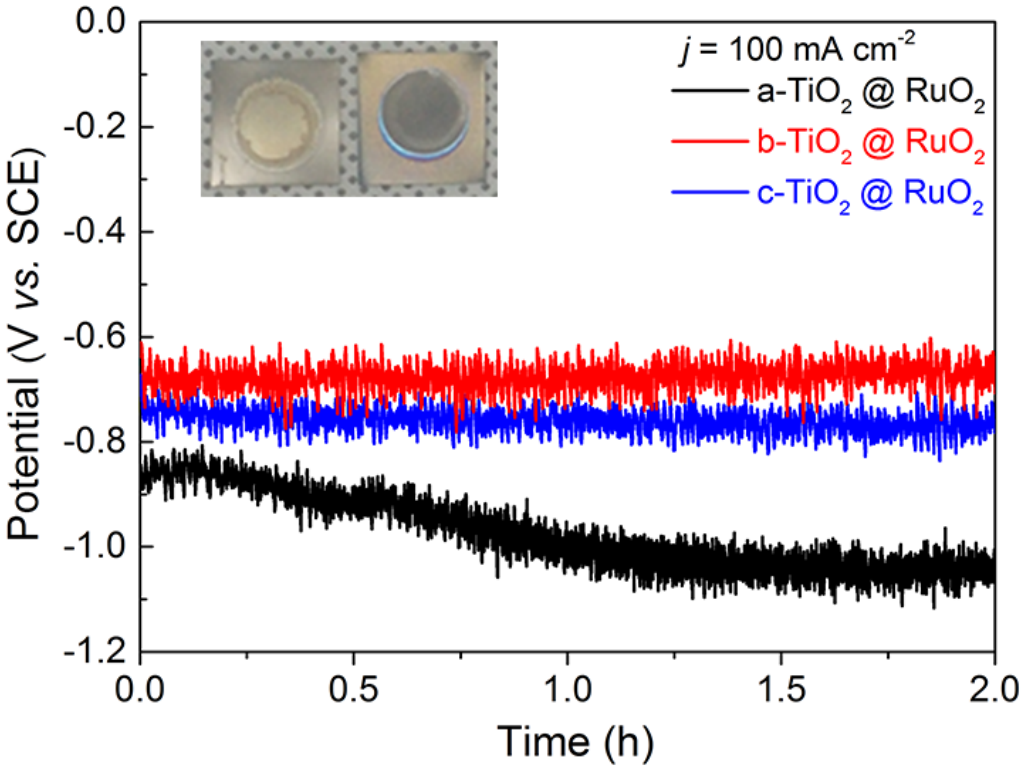

Figure 36. stability test comparison between two samples and their optical images.

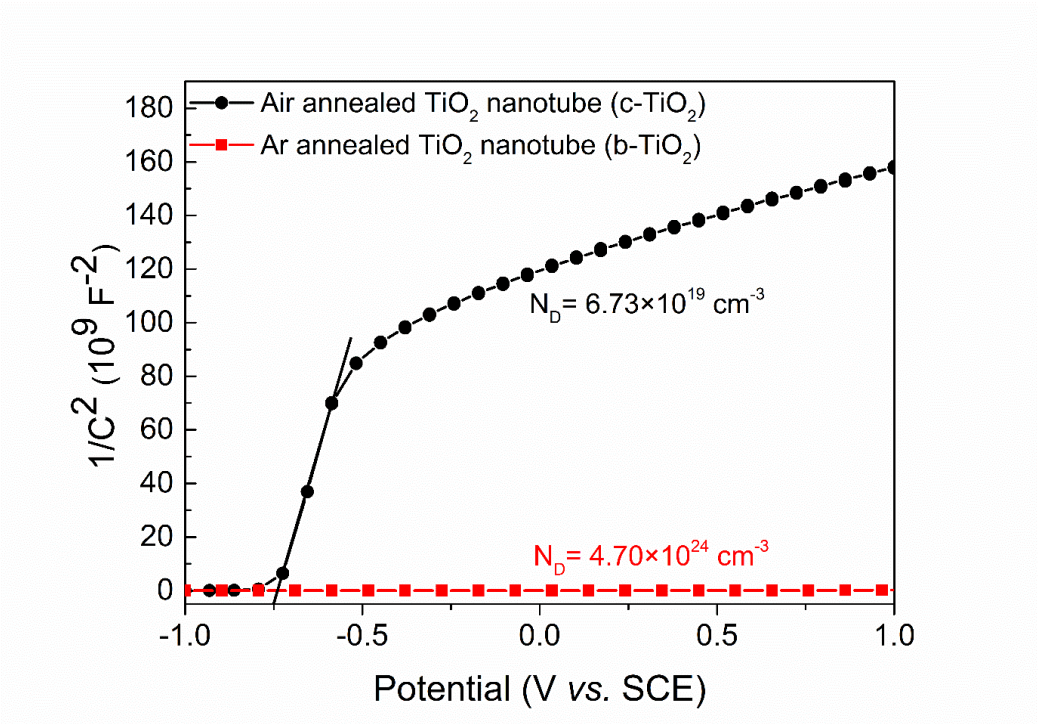

Figure 37. Mott-Schottky plot at a fixed frequency of 1kHz on annealed TiO_2 NTAs.

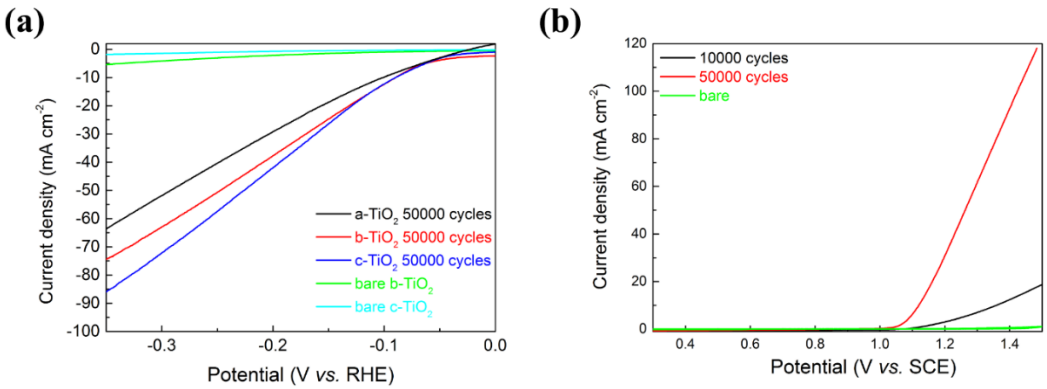

Figure 38. LSV scan of b-TiO_2@RuO_2 NTAs in a) 0.5M H_2SO_4 with scan rate 10mV/s. b) 5M NaCl (pH=2) with scan rate 10mV/s

material	η_{10mA/cm^2}	η_{100mA/cm^2}	synthesis condition	evaluation condition	ref
Ti/RuO_2	-	447mV	thermal decomposition	5M NaCl, pH=2, RT	[126]
macroporous TiO_2/RuO_2	-	270mV	thermal decomposition method with several sizes of PS microspheres	5M NaCl, pH=2, RT	[127]
$Ti/TiO_2/RuO_2$	184mV	-	spray pyrolysis	5M NaCl, pH=2, RT	[128]
$Ti/Ru_{0.3}Ti_{0.7}O_2$	360mV	-	-	3.5g/L NaCl	[129]
mesoporous TiO_2/RuO_2	436mV	676mV	pore templating with micelles of amphiphilic block-copolymers	4M NaCl, pH=3, 40℃	[130]
Ti/RuO_2	111mV	-	thermal decomposition	5M NaCl, 30℃	[131]
$Ti/TiO_2/RuO_2/SnO_2$	160mV	-	painting/baking	5M NaCl, 20℃	[132]
Ti/RuO_2	120mV	-	sol-gel	5M NaCl, pH=2, RT	[133]
$Ti/TiO_2/RuO_2$	131mV	-	sol-gel	5M NaCl, pH=2, RT	[134]
$Ti/TiO_2/RuO_2/CeO_2$	140mV	-	thermal decomposition	5M NaCl, pH=2, RT	[135]
Ti–Ru–Ir-based dimensionally stable anode	134mV	453mV	purchased by Bayer Materials, Leverkusen, Germany	4M NaCl, pH=2, RT	[136]
Ti/TiO_2 NTAs/RuO_2	130mV	425mV	electrochemical process	5M NaCl, pH=2, RT	This work

Table 5. Compilation of CER performance metrics for Ru-based catalyst synthesized under different condition.

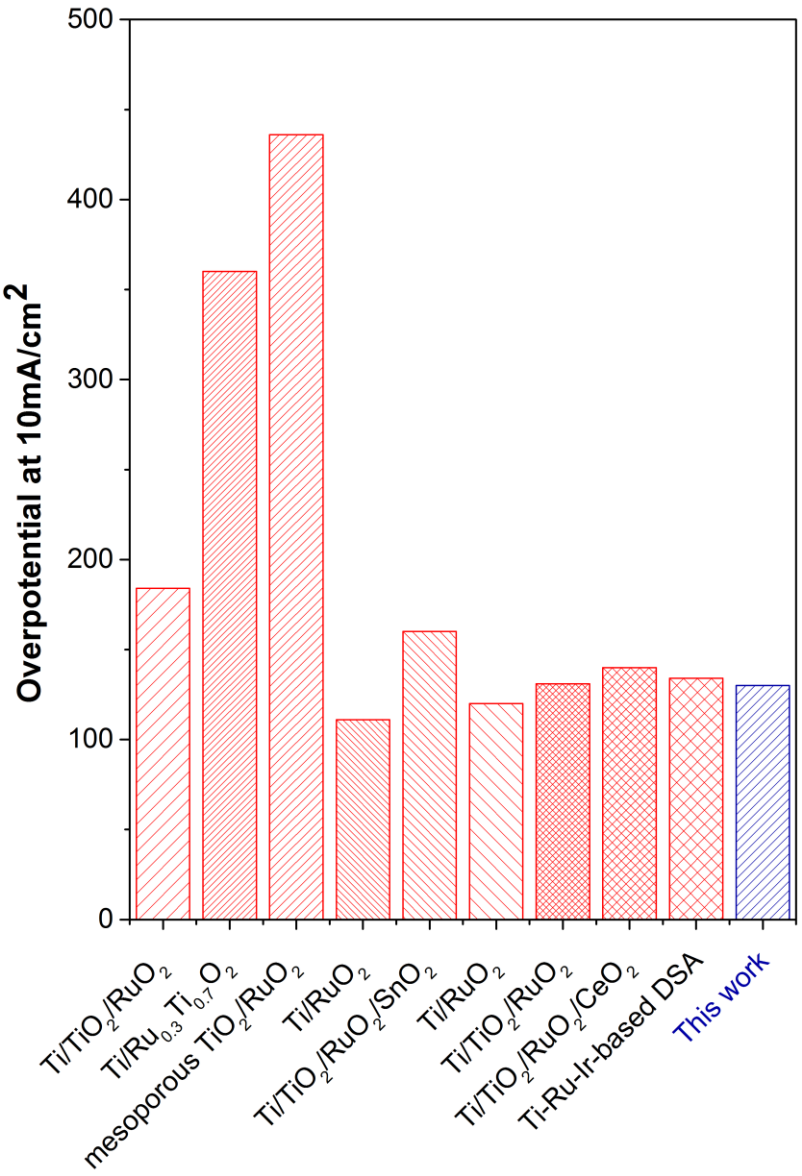

Figure 39. Comparison of CER overpotential at 10mA cm^{-2} with other Ru-based electrocatalyst reported in the literature.

	CER		HER	
material	performance	stability	performance	stability
a-TiO_2@RuO_2	O	O	O	X
b-TiO_2@RuO_2	O	O	O	O
c-TiO_2@RuO_2	X	-	O	O

Table 6. Summary of catalytic activity and stability of each TiO_2 NTAs@RuO_2 electrodes

3.3.2.2 Evaluation of conductivity under different bias

In order to investigate the more about the conductivity of the supporting electrode, cyclic voltammograms (CV) of the various supporting electrodes without RuO_2 using two different redox couples (**Figure 40**) were measured. Ferrocene and vanadium solutions were chosen for investigating CER (*i.e.* anodic potential) and HER (*i.e.* cathodic potential), respectively. As can be seen from Fig. 4a, all of the TiO_2 NTAs show clear V^{3+}/V^{2+} redox peaks with high current density regardless of the annealing condition, indicating that the electrical conductivity under cathodic potentials is good enough. This result is consistent with the observation that all samples show reasonable HER activity. On the other hand, the c-TiO_2 NTAs essentially no current under anodic potentials, indicating that the electrical conductivity is very poor. This result can explain why the RuO_2-loaded c-TiO_2 NTAs do not exhibit CER activity at all. It should be noted that the b-TiO_2 NTAs exhibit much larger current density and clear redox peaks, which must be very promising for CER. Such a different potential-dependence of the electrical conductivity between c-TiO_2 and b-TiO_2 can also be observed from the electrochemical impedance spectroscopy (EIS) shown in **Figure 41**. Furthermore, based on the obtained spectrum, equivalent circuit was constructed and fitting was performed, and electrochemical parameters were derived based on the circuit. The model we used is in **Figure 21b**, and recently other researchers fitted the impedance spectrum in a basic environment.[137] The shape and pattern of the spectrum were similar to those of this study, and similar values were obtained. As can be seen in **Table 7**, the resistance between the

barrier and the electrolyte is significantly reduced under the anodic region when the heat treatment is carried out in argon. On the other hand, under cathodic region, the resistance between the barrier and the electrolyte is similar, or the b-TiO_2 NTAs are slightly worse, which can be related to the slightly improved hydrogen evolution reaction activity of c-TIO_2 NTAs as shown in **Figure 38a**. The fact that the TiO_2 NTA has a large change in conductivity under anodic/cathodic voltage has been extensively investigated in other studies,[118] and representative results are attached to the **Figure 42**.

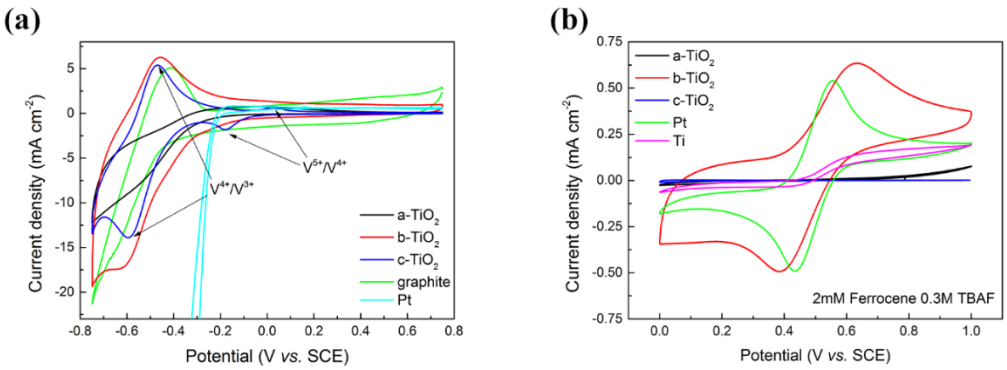

Figure 40. (a) CV scan of each TiO_2 substrate, Pt and graphite (electrolyte: 0.1M $VOSO_4$ supported by 3M H_2SO_4) (b) CV scan of each TiO_2 substrate, Pt and Ti (electrolyte: 2mM Ferrocene supported by TBAF)

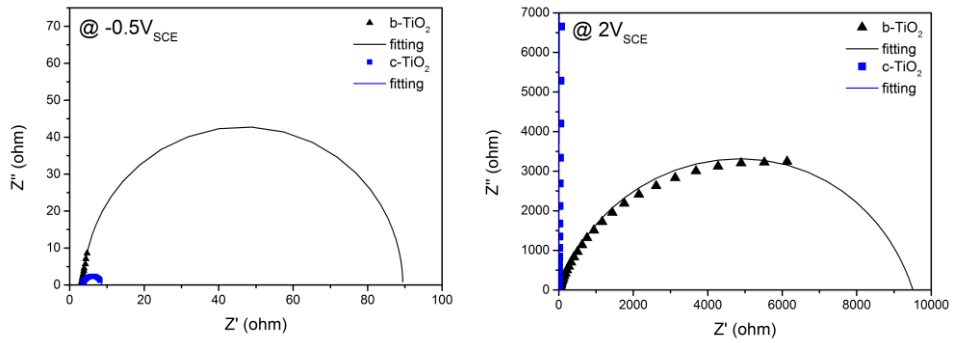

Figure 41. Electrochemical impedance spectroscopy. (a) Nyquist plot at -0.5V (*vs.* SCE) (b) Nyquist plots of the impedance data for c-TiO_2 and b-TiO_2 at 2V (*vs.* SCE)

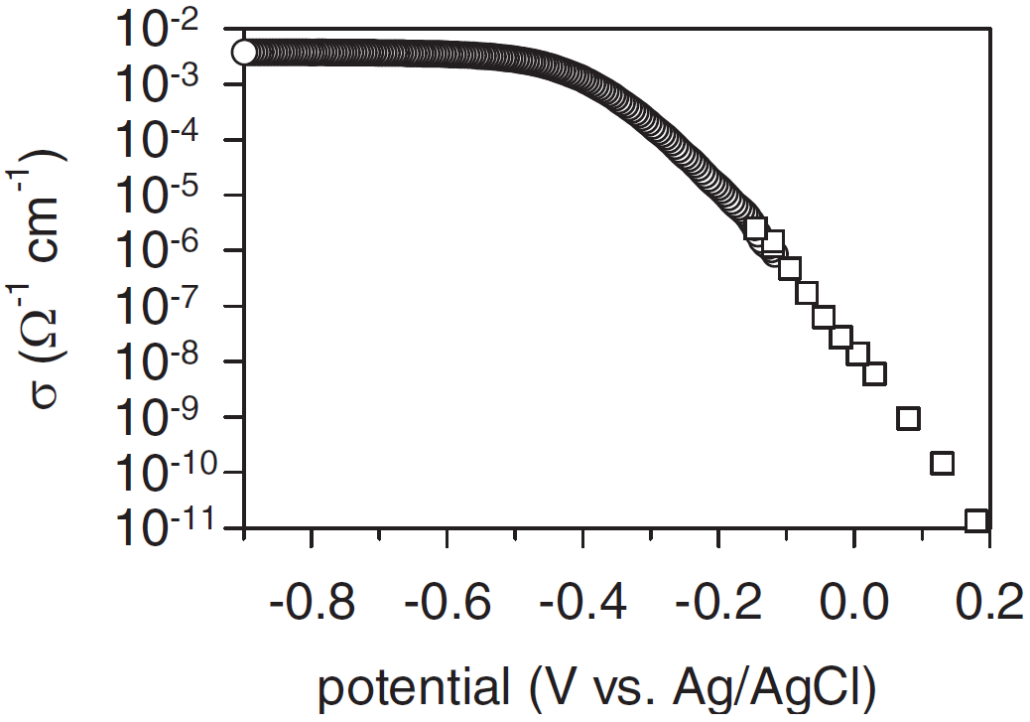

Figure 42. Electronic conductivity of TiO_2 NTAs obtained from EIS data under different bias (pH=2) [118]

Materials	applied voltage (V)	C_b(μF)	R_b(ohm)	C_i(μF)	R_i(ohm)
	2V	97.214	**8921**	1574.3	**584.1**
b-TiO_2	OCV (0.37V)	674	9983	195.8	40919
	-0.5V	14267	11.7	5294.3	74.53
	2V	3.0646	4651000	0.17936	7570100
c-TiO_2	OCV (0.29V)	234.02	14863	36.554	196030
	-0.5V	6820.5	2.487	8276.2	2.53

Table 7. Electrochemical parameters of TiO_2 NTAs electrode obtained by EIS.

4. Conclusions

The electro-catalytic performance of TiO_2 NTAs@RuO_2 for chlorine evolution was investigated. RuO_2 nanoparticle was successfully deposited onto TiO_2 NTAs by pulse electrodeposition. By varying the annealing condition of TiO_2 NTAs, electrochemical properties of TiO_2 NTAs were changed, affecting the catalytic properties. Because of inferior charge transfer property under anodic condition, c-TiO_2@RuO_2 electrode shows poor CER performance. On the other hand, Ar annealed b-TiO_2@RuO_2 electrode shows high performance in both HER and CER. This is ascribed to the decrease of charge transfer resistance. In order to make TiO_2 NTAs as good support material for universal potential, the use of Ar-annealed black TiO_2 is necessary.

References

1. Laird, T., Ullmann's Encyclopedia of Industrial Chemistry, VCH: Weinheim, Germany. 1996/1997. Section A, 28 vols. Section B, 8 vols. DM 19 400. ACS Publications: 1997.

2. O'Brien, T. F.; Bommaraju, T. V.; Hine, F., *Handbook of Chlor-Alkali Technology: Volume I: Fundamentals, Volume II: Brine Treatment and Cell Operation, Volume III: Facility Design and Product Handling, Volume IV: Operations, Volume V: Corrosion, Environmental Issues, and Future Developments*. Springer Science & Business Media: 2007; Vol. 1.

3. Chlor, E., Chlorine Industry Review, 2016−2017. euro chlor: 2017.

4. Fauvarque, J., The chlorine industry. *Pure and applied chemistry* **1996,** *68* (9), 1713-1720.

5. Schneider, F. L., Method for the continuous electrolytic production of chlorine for the sterilization of water. Google Patents: 1971.

6. Tsolaki, E.; Diamadopoulos, E., Technologies for ballast water treatment: a review. *Journal of Chemical technology and Biotechnology* **2010,** *85* (1), 19-32.

7. Hou, M.; Chen, L.; Guo, Z.; Dong, X.; Wang, Y.; Xia, Y., A clean and membrane-free chlor-alkali process with decoupled Cl 2 and H 2/NaOH production. *Nature communications* **2018,** *9* (1), 438.

8. Karlsson, R. K.; Cornell, A., Selectivity between oxygen and chlorine evolution in the chlor-alkali and chlorate processes. *Chemical reviews* **2016,** *116* (5), 2982-3028.

9. Exner, K. S.; Anton, J.; Jacob, T.; Over, H., Full Kinetics from First Principles of the Chlorine Evolution Reaction over a RuO2 (110) Model Electrode. *Angewandte Chemie International Edition* **2016,** *55* (26), 7501-7504.

10. Exner, K. S.; Sohrabnejad-Eskan, I.; Anton, J.; Jacob, T.; Over, H., Full Free Energy Diagram of an Electrocatalytic Reaction over a Single-Crystalline Model Electrode. *ChemElectroChem* **2017,** *4* (11), 2902-2908.

11. Consonni, V.; Trasatti, S.; Pollak, F.; O'Grady, W., Mechanism of chlorine evolution on oxide anodes study of pH effects. *Journal of electroanalytical chemistry and interfacial electrochemistry* **1987,** *228* (1-2), 393-406.

12. Guerrini, E.; Consonni, V.; Trasatti, S., Surface and electrocatalytic properties of well-defined and vicinal RuO 2 single crystal faces. *Journal of Solid State Electrochemistry* **2005,** *9* (5), 320-329.

13. Makarychev, Y.; Spasskaya, E.; Khodkevich, S.; Yakimenko, L., Corrosion Resistance of Oxidized Ru(and Ti) Anodes Containing Various Amounts of RuO 2 and TiO 2 in the Surface Coating. *Elektrokhimiya* **1976,** *12* (6), 994-997.

14. Pecherskii, M.; Gorodetskii, V.; Bune, N., The Kinetics of Secondary Electrode Processes on Ruthenium--Titanium Anodes in Chloride Solutions. *Elektrokhimiya* **1982,** *18* (3), 415-422.

15. Trasatti, S., Progress in the understanding of the mechanism of chlorine evolution at oxide electrodes. *Electrochimica acta* **1987,** *32* (3), 369-382.

16. Over, H., Atomic scale insights into electrochemical versus gas phase oxidation of HCl over RuO2-based catalysts: A comparative review. *Electrochimica Acta* **2013,** *93*, 314-333.

17. 김지예; 김춘수; 김성환; 윤제용, 총 설: DSA 전극에서 염소 발생 메커니즘. *Korean Chem. Eng. Res.(화학공학)* **2015,** *53* (5), 531-539.

18. Bergner, D., Reduction of by-product formation in alkali chloride membrane electrolysis. *Journal of Applied Electrochemistry* **1990,** *20* (5), 716-722.

19. Gorodetskii, V.; Pecherskii, M.; Yanke, V.; Bune, N. Y.; BUSSEMACHUKAS, V.; Kubasov, V.; Losev, V., Effect of Acidity on the Electrochemical and Corrosion Behavior of Titanium-ruthenium Oxide Anodes in Chloride Solutions. *SOVIET ELECTROCHEMISTRY* **1981,** *17* (4), 421-425.

20. Furlong, D.; Yates, D.; Healy, T.; Trasatti, S., Electrodes of conductive metallic oxides, Part B. Elsevier, Amsterdam: 1981.

21. Arikawa, T.; Murakami, Y.; Takasu, Y., Simultaneous determination of chlorine and oxygen evolving at RuO2/Ti and RuO2–TiO2/Ti anodes by differential electrochemical mass spectroscopy. *Journal of Applied Electrochemistry* **1998,** *28* (5), 511-516.

22. Pourbaix, M., *Atlas of electrochemical equilibria in aqueous solutions*. Pergamon: 1966; Vol. 1.

23. Loučka, T., The potential-pH diagram for the Ru− H 2 O− Cl− system at 25° C. *Journal of Applied Electrochemistry* **1990,** *20* (3), 522-523.

24. Holmin, S.; Näslund, L.-Å.; Ingason, Á. S.; Rosen, J.; Zimmerman, E., Corrosion of ruthenium dioxide based cathodes in alkaline medium caused by reverse currents. *Electrochimica Acta* **2014,** *146*, 30-36.

25. Kuznetsova, E.; Petrykin, V.; Sunde, S.; Krtil, P., Selectivity of Nanocrystalline IrO 2-Based Catalysts in Parallel Chlorine and Oxygen Evolution. *Electrocatalysis* **2015,** *6* (2), 198-210.

26. Caldwell, D.; Hazelrigg, M.; Coulter, M., Modern Chlor–Alkali Technology. *Modern Chlor-Alkali Technology* **1980**.

27. Makarova, M. V.; Jirkovský, J.; Klementová, M.; Jirka, I.; Macounová, K.; Krtil, P., The electrocatalytic behavior of Ru0. 8Co0. 2O2− x—the effect of particle shape and surface composition. *Electrochimica Acta* **2008,** *53* (5), 2656-2664.

28. Xiong, K.; Deng, Z.; Li, L.; Chen, S.; Xia, M.; Zhang, L.; Qi, X.; Ding, W.; Tan, S.; Wei, Z., Sn and Sb co-doped RuTi oxides supported on TiO 2 nanotubes anode for selectivity toward electrocatalytic chlorine evolution. *Journal of Applied Electrochemistry* **2013,** *43* (8), 847-854.

29. Wang, S.; Xu, H.; Yao, P.; Chen, X., Ti/RuO2-IrO2-SnO2-Sb2O5 Anodes for Cl2 Evolution from Seawater. *Electrochemistry* **2012,** *80* (7), 507-511.

30. Chen, S.; Zheng, Y.; Wang, S.; Chen, X., Ti/RuO2–Sb2O5–SnO2 electrodes for chlorine evolution from seawater. *Chemical Engineering Journal* **2011,** *172* (1), 47-51.

31. Trasatti, S., Electrocatalysis in the anodic evolution of oxygen and chlorine. *Electrochimica Acta* **1984,** *29* (11), 1503-1512.

32. Petrykin, V.; Macounova, K.; Shlyakhtin, O.; Krtil, P., Tailoring the selectivity for electrocatalytic oxygen evolution on ruthenium oxides by zinc substitution. *Angewandte Chemie International Edition* **2010,** *49* (28), 4813-4815.

33. Petrykin, V.; Macounova, K.; Franc, J.; Shlyakhtin, O.; Klementova, M.; Mukerjee, S.; Krtil, P., Zn-Doped RuO2 electrocatalyts for Selective Oxygen Evolution: Relationship between Local Structure and Electrocatalytic Behavior in Chloride Containing Media. *Chemistry of Materials* **2010,** *23* (2), 200-207.

34. Macounová, K.; Makarova, M.; Jirkovský, J.; Franc, J.; Krtil, P., Parallel oxygen and chlorine evolution on Ru1− xNixO2− y nanostructured electrodes. *Electrochimica Acta* **2008,** *53* (21), 6126-6134.

35. Abbott, D. F.; Petrykin, V.; Okube, M.; Bastl, Z.; Mukerjee, S.; Krtil, P., Selective Chlorine Evolution Catalysts Based on Mg-Doped Nanoparticulate Ruthenium Dioxide. *Journal of The Electrochemical Society* **2015,** *162* (1), H23-H31.

36. Tilak, B.; Tari, K.; Hoover, C., Metal Anodes and Hydrogen Cathodes: Their Activity Towards O 2 Evolution and ClO3− Reduction Reactions. *Journal of The Electrochemical Society* **1988,** *135* (6), 1386-1392.

37. Pfaff, G.; Reynders, P., Angle-dependent optical effects deriving from submicron structures of films and pigments. *Chemical reviews* **1999,** *99* (7), 1963-1982.

38. Salvador, A.; Pascual-Martı, M.; Adell, J.; Requeni, A.; March, J., Analytical methodologies for atomic spectrometric determination of metallic oxides in UV sunscreen creams. *Journal of pharmaceutical and biomedical analysis* **2000,** *22* (2), 301-306.

39. Zallen, R.; Moret, M., The optical absorption edge of brookite TiO2. *Solid State Communications* **2006,** *137* (3), 154-157.

40. Braun, J. H.; Baidins, A.; Marganski, R. E., TiO2 pigment technology: a review. *Progress in organic coatings* **1992,** *20* (2), 105-138.

41. Yuan, S.; Chen, W.; Hu, S., Fabrication of TiO2 nanoparticles/surfactant polymer complex film on glassy carbon electrode and its application to sensing trace dopamine. *Materials Science and Engineering: C* **2005,** *25* (4), 479-485.

42. Fujishima, A.; Honda, K., Electrochemical photolysis of water at a semiconductor electrode. *nature* **1972,** *238* (5358), 37.

43. Hanaor, D. A.; Sorrell, C. C., Review of the anatase to rutile phase transformation. *Journal of Materials science* **2011,** *46* (4), 855-874.

44. Muscat, J.; Swamy, V.; Harrison, N. M., First-principles calculations of the phase stability of TiO 2. *Physical Review B* **2002,** *65* (22), 224112.

45. Fernandez-Garcia, M.; Martinez-Arias, A.; Hanson, J.; Rodriguez, J., Nanostructured oxides in chemistry: characterization and properties. *Chemical Reviews* **2004,** *104* (9), 4063-4104.

46. Lee, K.; Mazare, A.; Schmuki, P., One-dimensional titanium dioxide nanomaterials: nanotubes. *Chemical Reviews* **2014,** *114* (19), 9385-9454.

47. Albu, S. P.; Ghicov, A.; Aldabergenova, S.; Drechsel, P.; LeClere, D.; Thompson, G. E.; Macak, J. M.; Schmuki, P., Formation of Double-Walled TiO2 Nanotubes and Robust Anatase Membranes. *Advanced Materials* **2008,** *20* (21), 4135-4139.

48. Jin, B.; Zhou, X.; Huang, L.; Lickleder, M.; Yang, M.; Schmuki, P., Aligned MoOx/MoS2 Core–Shell Nanotubular Structures with a High Density of Reactive Sites Based on Self-Ordered Anodic Molybdenum Oxide Nanotubes. *Angewandte Chemie International Edition* **2016,** *55* (40), 12252-12256.

49. Bauer, S.; Pittrof, A.; Tsuchiya, H.; Schmuki, P., Size-effects in TiO2 nanotubes: Diameter dependent anatase/rutile stabilization. *Electrochemistry Communications* **2011,** *13* (6), 538-541.

50. Wang, X.; Li, Z.; Shi, J.; Yu, Y., One-dimensional titanium dioxide nanomaterials: nanowires, nanorods, and nanobelts. *Chemical reviews* **2014,** *114* (19), 9346-9384.

51. Landmann, M.; Rauls, E.; Schmidt, W., The electronic structure and optical response of rutile, anatase and brookite TiO2. *Journal of physics: condensed matter* **2012,** *24* (19), 195503.

52. Bummel, T., Über Wachstum und Aufbau elektrolytisch erzeugter Aluminiumoxydschichten. *Zeitschrift für Physik* **1936,** *99* (7-8), 518-551.

53. Baumann, W., Wechselstromuntersuchungen an anodisch oxydiertem Aluminium. *Zeitschrift für Physik* **1936,** *102* (1-2), 59-66.

54. Chen, X.; Pomerantseva, E.; Banerjee, P.; Gregorczyk, K.; Ghodssi, R.; Rubloff, G., Ozone-based atomic layer deposition of crystalline V2O5 films for high performance electrochemical energy storage. *Chemistry of Materials* **2012,** *24* (7), 1255-1261.

55. Bae, C.; Yoon, Y.; Yoon, W.-S.; Moon, J.; Kim, J.; Shin, H., Hierarchical titania nanotubes with self-branched crystalline nanorods. *ACS applied materials & interfaces* **2010,** *2* (6), 1581-1587.

56. Honda, K.; Rao, T. N.; Tryk, D.; Fujishima, A.; Watanabe, M.; Yasui, K.; Masuda, H., Electrochemical Characterization of the Nanoporous Honeycomb Diamond Electrode as an Electrical Double-Layer Capacitor. *Journal of The Electrochemical Society* **2000,** *147* (2), 659-664.

57. Martinson, A. B.; Elam, J. W.; Hupp, J. T.; Pellin, M. J., ZnO nanotube based dye-sensitized solar cells. *Nano letters* **2007,** *7* (8), 2183-2187.

58. Foong, T. R.; Shen, Y.; Hu, X.; Sellinger, A., Template-directed liquid ALD growth of TiO2 nanotube arrays: properties and potential in photovoltaic devices. *Advanced Functional Materials* **2010,** *20* (9), 1390-1396.

59. Jones, M. R.; Osberg, K. D.; Macfarlane, R. J.; Langille, M. R.; Mirkin, C. A., Templated techniques for the synthesis and assembly of plasmonic nanostructures. *Chemical Reviews* **2011,** *111* (6), 3736-3827.

60. Nakao, M.; Oku, S.; Tanaka, H.; Shibata, Y.; Yokoo, A.; Tamamura, T.; Masuda, H., Fabrication of GaAs hole array as a 2D-photonic crystal and their application to photonic bandgap waveguide. *Optical and quantum electronics* **2002,** *34* (1-3), 183-193.

61. Lee, S. B.; Mitchell, D. T.; Trofin, L.; Nevanen, T. K.; Söderlund, H.; Martin, C. R., Antibody-based bio-nanotube membranes for enantiomeric drug separations. *Science* **2002,** *296* (5576), 2198-2200.

62. Jain, P.; Sun, L.; Dai, J.; Baker, G. L.; Bruening, M. L., High-capacity purification of his-tagged proteins by affinity membranes containing functionalized polymer brushes. *Biomacromolecules* **2007,** *8* (10), 3102-3107.

63. Zwilling, V.; Darque-Ceretti, E.; Boutry-Forveille, A.; David, D.; Perrin, M.-Y.; Aucouturier, M., Structure and physicochemistry of anodic oxide films on titanium and TA6V alloy. *Surface and Interface Analysis* **1999,** *27* (7), 629-637.

64. Berger, S.; Jakubka, F.; Schmuki, P., Self-ordered hexagonal nanoporous hafnium oxide and transition to aligned HfO2 nanotube layers. *Electrochemical and Solid-State Letters* **2009,** *12* (7), K45-K48.

65. Hahn, R.; Macak, J.; Schmuki, P., Rapid anodic growth of TiO2 and WO3 nanotubes in fluoride free electrolytes. *Electrochemistry Communications* **2007,** *9* (5), 947-952.

66. Wei, W.; Lee, K.; Shaw, S.; Schmuki, P., Anodic formation of high aspect ratio, self-ordered Nb 2 O 5 nanotubes. *Chemical Communications* **2012,** *48* (35), 4244-4246.

67. Berger, S.; Jakubka, F.; Schmuki, P., Formation of hexagonally ordered nanoporous anodic zirconia. *Electrochemistry Communications* **2008,** *10* (12), 1916-1919.

68. Albu, S. P.; Ghicov, A.; Schmuki, P., High aspect ratio, self-ordered iron oxide nanopores formed by anodization of Fe in ethylene glycol/NH4F electrolytes. *physica status solidi (RRL)-Rapid Research Letters* **2009,** *3* (2-3), 64-66.

69. Nah, Y.-C.; Shrestha, N. K.; Kim, D.; Schmuki, P., Electrochemical growth of self-organized TiO 2–WO 3 composite nanotube layers: effects of applied voltage and time. *Journal of Applied Electrochemistry* **2013,** *43* (1), 9-13.

70. Regonini, D.; Bowen, C. R.; Jaroenworaluck, A.; Stevens, R., A review of growth mechanism, structure and crystallinity of anodized TiO2 nanotubes. *Materials Science and Engineering: R: Reports* **2013,** *74* (12), 377-406.

71. Riboni, F.; Nguyen, N. T.; So, S.; Schmuki, P., Aligned metal oxide nanotube arrays: key-aspects of anodic TiO 2 nanotube formation and properties. *Nanoscale Horizons* **2016,** *1* (6), 445-466.

72. Güntherschulze, A.; Betz, H., Die Bewegung der Ionengitter von Isolatoren bei extremen elektrischen Feldstärken. *Zeitschrift für Physik* **1934,** *92* (5-6), 367-374.

73. Yasuda, K.; Macak, J. M.; Berger, S.; Ghicov, A.; Schmuki, P., Mechanistic aspects of the self-organization process for oxide nanotube formation on valve metals. *Journal of the electrochemical society* **2007,** *154* (9), C472-C478.

74. Park, J.; Bauer, S.; von der Mark, K.; Schmuki, P., Nanosize and vitality: TiO2 nanotube diameter directs cell fate. *Nano letters* **2007,** *7* (6), 1686-1691.

75. Albu, S. P.; Schmuki, P., TiO2 nanotubes grown in different organic electrolytes: Two-size self-organization, single vs. double-walled tubes, and giant diameters. *physica status solidi (RRL)-Rapid Research Letters* **2010,** *4* (8-9), 215-217.

76. Mirabolghasemi, H.; Liu, N.; Lee, K.; Schmuki, P., Formation of 'single walled'TiO 2 nanotubes with significantly enhanced electronic properties for higher efficiency dye-sensitized solar cells. *Chemical Communications* **2013,** *49* (20), 2067-2069.

77. Ruff, T.; Hahn, R.; Schmuki, P., From anodic TiO2 nanotubes to hexagonally ordered TiO2 nanocolumns. *Applied Surface Science* **2011,** *257* (19), 8177-8181.

78. So, S.; Lee, K.; Schmuki, P., Ultrafast growth of highly ordered anodic TiO2 nanotubes in lactic acid electrolytes. *Journal of the American Chemical Society* **2012,** *134* (28), 11316-11318.

79. Banerjee, S.; Misra, M.; Mohapatra, S. K.; Howard, C.; Mohapatra, S. K.; Kamilla, S. K., Formation of chelating agent driven anodized TiO2 nanotubular membrane and its photovoltaic application. *Nanotechnology* **2010,** *21* (14), 145201.

80. Macak, J.; Hildebrand, H.; Marten-Jahns, U.; Schmuki, P., Mechanistic aspects and growth of large diameter self-organized TiO2 nanotubes. *Journal of Electroanalytical Chemistry* **2008,** *621* (2), 254-266.

81. Li, S.; Zhang, G.; Guo, D.; Yu, L.; Zhang, W., Anodization fabrication of highly ordered TiO2 nanotubes. *The Journal of Physical Chemistry C* **2009,** *113* (29), 12759-12765.

82. Lee, K.; Kim, J.; Kim, H.; Lee, Y.; Tak, Y.; Kim, D.; Schmuki, P., Effect of electrolyte conductivity on the formation of a nanotubular TiO2 photoanode for a dye-sensitized solar cell. *Journal of Korean Physical Society* **2009,** *54*, 1027.

83. Regonini, D.; Satka, A.; Jaroenworaluck, A.; Allsopp, D. W.; Bowen, C. R.; Stevens, R., Factors influencing surface morphology of anodized TiO2 nanotubes. *Electrochimica Acta* **2012,** *74*, 244-253.

84. Macak, J. M.; Albu, S. P.; Schmuki, P., Towards ideal hexagonal self-ordering of TiO2 nanotubes. *physica status solidi (RRL)-Rapid Research Letters* **2007,** *1* (5), 181-183.

85. Zhang, L.; Cho, H.; Li, F.; Metzger, R.; Doyle, W., Cellular growth of highly ordered porous anodic films on aluminium. *Journal of materials science letters* **1998,** *17* (4), 291-294.

86. Chen, B.; Lu, K.; Geldmeier, J. A., Highly ordered titania nanotube arrays with square, triangular, and sunflower structures. *Chemical Communications* **2011,** *47* (36), 10085-10087.

87. Kondo, T.; Nagao, S.; Yanagishita, T.; Nguyen, N. T.; Lee, K.; Schmuki, P.; Masuda, H., Ideally ordered porous TiO2 prepared by anodization of pretextured Ti by nanoimprinting process. *Electrochemistry Communications* **2015,** *50*, 73-76.

88. Schodek, D. L.; Ferreira, P.; Ashby, M. F., *Nanomaterials, nanotechnologies and design: an introduction for engineers and architects*. Butterworth-Heinemann: 2009.

89. Sulka, G. D.; Zaraska, L.; Stepniowski, W. J., Anodic porous alumina as a template for nanofabrication. In *Encyclopedia of nanoscience and nanotechnology*, American Scientific Publishers: 2011; Vol. 11, pp 261-349.

90. Bauer, S.; Kleber, S.; Schmuki, P., TiO2 nanotubes: Tailoring the geometry in H3PO4/HF electrolytes. *Electrochemistry Communications* **2006,** *8* (8), 1321-1325.

91. Tang, H.; Prasad, K.; Sanjines, R.; Schmid, P.; Levy, F., Electrical and optical properties of TiO2 anatase thin films. *Journal of applied physics* **1994,** *75* (4), 2042-2047.

92. Forro, L.; Chauvet, O.; Emin, D.; Zuppiroli, L.; Berger, H.; Levy, F., High mobility n-type charge carriers in large single crystals of anatase (TiO2). *Journal of Applied Physics* **1994,** *75* (1), 633-635.

93. Kuang, D.; Brillet, J.; Chen, P.; Takata, M.; Uchida, S.; Miura, H.; Sumioka, K.; Zakeeruddin, S. M.; Grätzel, M., Application of highly ordered TiO2 nanotube arrays in flexible dye-sensitized solar cells. *ACS nano* **2008,** *2* (6), 1113-1116.

94. Chen, S.; Paulose, M.; Ruan, C.; Mor, G. K.; Varghese, O. K.; Kouzoudis, D.; Grimes, C. A., Electrochemically synthesized CdS nanoparticle-modified TiO2 nanotube-array photoelectrodes: preparation, characterization, and application to photoelectrochemical cells. *Journal of Photochemistry and Photobiology A: Chemistry* **2006,** *177* (2-3), 177-184.

95. Ginley, D.; Knotek, M., Hydrogen in TiO2 Photoanodes. *Journal of the Electrochemical Society* **1979,** *126* (12), 2163-2166.

96. Sekiya, T.; Yagisawa, T.; Kamiya, N.; Das Mulmi, D.; Kurita, S.; Murakami, Y.; Kodaira, T., Defects in anatase TiO2 single crystal controlled by heat treatments. *Journal of the Physical Society of Japan* **2004,** *73* (3), 703-710.

97. Lin, T.; Yang, C.; Wang, Z.; Yin, H.; Lü, X.; Huang, F.; Lin, J.; Xie, X.; Jiang, M., Effective nonmetal incorporation in black titania with enhanced solar energy utilization. *Energy & Environmental Science* **2014,** *7* (3), 967-972.

98. Chen, X.; Liu, L.; Peter, Y. Y.; Mao, S. S., Increasing solar absorption for photocatalysis with black hydrogenated titanium dioxide nanocrystals. *Science* **2011,** *331* (6018), 746-750.

99. Cui, H.; Zhao, W.; Yang, C.; Yin, H.; Lin, T.; Shan, Y.; Xie, Y.; Gu, H.; Huang, F., Black TiO2 nanotube arrays for high-efficiency photoelectrochemical water-splitting. *Journal of Materials Chemistry A* **2014,** *2* (23), 8612-8616.

100. Amano, F.; Nakata, M., High-temperature calcination and hydrogen reduction of rutile TiO2: A method to improve the photocatalytic activity for water oxidation. *Applied Catalysis B: Environmental* **2014,** *158*, 202-208.

101. Lu, X.; Wang, G.; Zhai, T.; Yu, M.; Gan, J.; Tong, Y.; Li, Y., Hydrogenated TiO2 nanotube arrays for supercapacitors. *Nano letters* **2012,** *12* (3), 1690-1696.

102. Shah, M. W.; Zhu, Y.; Fan, X.; Zhao, J.; Li, Y.; Asim, S.; Wang, C., Facile synthesis of defective TiO 2− x nanocrystals with high surface area and tailoring bandgap for visible-light photocatalysis. *Scientific reports* **2015,** *5*, 15804.

103. Stiller, M.; Barzola-Quiquia, J.; Lorite, I.; Esquinazi, P.; Kirchgeorg, R.; Albu, S. P.; Schmuki, P., Transport properties of single TiO2 nanotubes. *Applied Physics Letters* **2013,** *103* (17), 173108.

104. Tighineanu, A.; Albu, S. P.; Schmuki, P., Conductivity of anodic TiO2 nanotubes: Influence of annealing conditions. *physica status solidi (RRL)-Rapid Research Letters* **2014,** *8* (2), 158-162.

105. Huber, B.; Gnaser, H.; Ziegler, C., Electrical properties of nanocrystalline anatase TiO2 thin films with different crystallite size. *Surface science* **2004,** *566*, 419-424.

106. Akl, A.; Kamal, H.; Abdel-Hady, K., Fabrication and characterization of sputtered titanium dioxide films. *Applied surface science* **2006,** *252* (24), 8651-8656.

107. Chen, Z.; Cummins, D.; Reinecke, B. N.; Clark, E.; Sunkara, M. K.; Jaramillo, T. F., Core–shell MoO3–MoS2 nanowires for hydrogen evolution: a functional design for electrocatalytic materials. *Nano letters* **2011,** *11* (10), 4168-4175.

108. Chang, B.-Y.; Park, S.-M., Electrochemical impedance spectroscopy. *Annual Review of Analytical Chemistry* **2010,** *3*, 207-229.

109. Muñoz, A.; Chen, Q.; Schmuki, P., Interfacial properties of self-organized TiO 2 nanotubes studied by impedance spectroscopy. *Journal of Solid State Electrochemistry* **2007,** *11* (8), 1077-1084.

110. Pan, J.; Thierry, D.; Leygraf, C., Electrochemical impedance spectroscopy study of the passive oxide film on titanium for implant application. *Electrochimica Acta* **1996,** *41* (7-8), 1143-1153.

111. Roy, P.; Berger, S.; Schmuki, P., TiO2 nanotubes: synthesis and applications. *Angewandte Chemie International Edition* **2011,** *50* (13), 2904-2939.

112. Zhitomirsky, I.; Gal-Or, L., Ruthenium oxide deposits prepared by cathodic electrosynthesis. *Materials Letters* **1997,** *31* (1-2), 155-159.

113. Hu, C.-C.; Chang, K.-H., Cyclic voltammetric deposition of hydrous ruthenium oxide for electrochemical capacitors: effects of codepositing iridium oxide. *Electrochimica Acta* **2000,** *45* (17), 2685-2696.

114. Sugawara, Y.; Yadav, A.; Nishikata, A.; Tsuru, T., EQCM study on dissolution of ruthenium in sulfuric acid. *Journal of the Electrochemical Society* **2008,** *155* (9), B897-B902.

115. Puippe, J.-C.; Leaman, F., *Theory and practice of pulse plating*. Amer Electroplaters Soc: 1986.

116. Chandrasekar, M.; Pushpavanam, M., Pulse and pulse reverse plating—Conceptual, advantages and applications. *Electrochimica Acta* **2008,** *53* (8), 3313-3322.

117. Roy, S.; Landolt, D., Determination of the practical range of parameters during reverse-pulse current plating. *Journal of Applied Electrochemistry* **1997,** *27* (3), 299-307.

118. Abayev, I.; Zaban, A.; Fabregat-Santiago, F.; Bisquert, J., Electronic conductivity in nanostructured TiO2 films permeated with electrolyte. *physica status solidi (a)* **2003,** *196* (1).

119. Morgan, D. J., Resolving ruthenium: XPS studies of common ruthenium materials. *Surf Interface Anal* **2015,** *47* (11), 1072-1079.

120. Cox, P. A.; Goodenough, J. B.; Tavener, P. J.; Telles, D.; Egdell, R. G., THE ELECTRONIC-STRUCTURE OF BI2-XGDXRU2O7 AND RUO2 - A STUDY BY ELECTRON-SPECTROSCOPY. *Journal of Solid State Chemistry* **1986,** *62* (3), 360-370.

121. Wang, W.; Guo, S. R.; Lee, I.; Ahmed, K.; Zhong, J. B.; Favors, Z.; Zaera, F.; Ozkan, M.; Ozkan, C. S., Hydrous Ruthenium Oxide Nanoparticles Anchored to Graphene and Carbon Nanotube Hybrid Foam for Supercapacitors. *Scientific Reports* **2014,** *4*.

122. Liu, C.; Li, C. L.; Ahmed, K.; Wang, W.; Lee, I.; Zaera, F.; Ozkan, C. S.; Ozkan, M., Scalable, Binderless, and Carbonless Hierarchical Ni Nanodendrite Foam Decorated with Hydrous Ruthenium Dioxide for 1.6 V Symmetric Supercapacitors. *Advanced Materials Interfaces* **2016,** *3* (6).

123. Yang, Y.; Kao, L. C.; Liu, Y.; Sun, K.; Yu, H.; Guo, J.; Liou, S. Y. H.; Hoffmann, M. R., Cobalt-Doped Black TiO2 Nanotube Array as a Stable Anode for Oxygen Evolution and Electrochemical Wastewater Treatment. *ACS catalysis* **2018,** *8*, 4278-4287.

124. Ge, M. Z.; Li, Q. S.; Cao, C. Y.; Huang, J. Y.; Li, S. H.; Zhang, S. N.; Chen, Z.; Zhang, K. Q.; Al-Deyab, S. S.; Lai, Y. K., One-dimensional TiO2 Nanotube Photocatalysts for Solar Water Splitting. *Advanced Science* **2017,** *4* (1).

125. Hazra, A.; Bhowmik, B.; Dutta, K.; Chattopadhyay, P. P.; Bhattacharyya, P., Stoichiometry, Length, and Wall Thickness Optimization of TiO2 Nanotube Array for Efficient Alcohol Sensing. *Acs Applied Materials & Interfaces* **2015,** *7* (18), 9336-9348.

126. Luu, T. L.; Kim, C.; Kim, J.; Kim, S.; Yoon, J., The Effect of Preparation Parameters in Thermal Decomposition of Ruthenium Dioxide Electrodes on Chlorine Electro-Catalytic Activity. *Bulletin of the Korean Chemical Society* **2015,** *36* (5), 1411-1417.

127. Luu, T. L.; Kim, C.; Kim, S.; Kim, J.; Yoon, J., Fabricating macroporous RuO2-TiO2 electrodes using polystyrene templates for high chlorine evolution efficiencies. *Desalination and Water Treatment* **2017,** *77*, 94-104.

128. Kosevic, M.; Stopic, S.; Bulan, A.; Kintrup, J.; Weber, R.; Stevanovic, J.; Panic, V.; Friedrich, B., A continuous process for the ultrasonic spray pyrolysis synthesis of RuO2/TiO2 particles and their application as a coating of activated titanium anode. *Advanced Powder Technology* **2017,** *28* (1), 43-49.

129. de Moura, D. C.; de Araujo, C. K. C.; Zanta, C.; Salazar, R.; Martinez-Huitle, C. A., Active chlorine species electrogenerated on Ti/Ru0.3Ti0.7O2 surface: Electrochemical behavior, concentration determination and their application. *Journal of Electroanalytical Chemistry* **2014,** *731*, 145-152.

130. Menzel, N.; Ortel, E.; Mette, K.; Kraehnert, R.; Strasser, P., Dimensionally Stable Ru/Ir/TiO2-Anodes with Tailored Mesoporosity for Efficient Electrochemical Chlorine Evolution. *Acs Catalysis* **2013,** *3* (6), 1324-1333.

131. Arikado, T.; Iwakura, C.; Tamura, H., Some oxide catalysts for the anodic evolution of chlorine: reaction mechanism and catalytic activity. *Electrochimica Acta* **1978,** *23* (1), 9-15.

132. Harrison, J. A.; Caldwell, D. L.; White, R. E., Electrocatalysis and the chlorine evolution reaction—II. Comparison of anode materials. *Electrochimica Acta* **1984,** *29* (2), 203-209.

133. Panić, V. V.; Dekanski, A. B.; Milonjić, S. K.; Mišković-Stanković, V. B.; Nikolić, B. Ž., Electrocatalytic activity of sol-gel-prepared RuO2/Ti anode in chlorine and oxygen evolution reactions. *Russian Journal of Electrochemistry* **2006,** *42* (10), 1055-1060.

134. Panic, V. V.; Nikolic, B. Z., Electrocatalytic properties and stability of titanium anodes activated by the inorganic sol-gel procedure. *Journal of the Serbian Chemical Society* **2008,** *73* (11), 1083-1112.

135. De Faria, L. A.; Boodts, J. F. C.; Trasatti, S., Electrocatalytic properties of Ru + Ti + Ce mixed oxide electrodes for the Cl2 evolution reaction. *Electrochimica Acta* **1997,** *42* (23), 3525-3530.

136. Zeradjanin, A. R.; Menzel, N.; Schuhmann, W.; Strasser, P., On the faradaic selectivity and the role of surface inhomogeneity during the chlorine evolution reaction on ternary Ti-Ru-Ir mixed metal oxide electrocatalysts. *Physical Chemistry Chemical Physics* **2014,** *16* (27), 13741-13747.

137. Yahia, S. A. A.; Hamadou, L.; Kadri, A.; Benbrahim, N.; Sutter, E., Effect of anodizing potential on the formation and EIS characteristics of TiO2 nanotube arrays. *Journal of The Electrochemical Society* **2012,** *159* (4), K83-K92.

Abstract in Korean

국 문 초 록

이산화 루테늄 (RuO_2)은 탈수소화 반응, 염산의 산화반응 및 클로로 알칼리(chlor-alkali) 공정과 같은 다양한 화학 반응에 널리 쓰이고 있다. 일반적으로, 이산화 루테늄계 촉매의 안정성을 향상시키기 위해, 이산화 티타늄(TiO_2)을 사용한다. 특히, 나노 구조는 촉매 활성 부위를 늘린다는 점에서 촉매 반응을 향상시키는데 많이 사용되었다. 그러나 전기 촉매 반응의 경우, 촉매를 담지 하는 담지체가 충분히 전도성이 있어서 산화 환원 반응에 필요한 전하를 전달할 수 있어야 한다. 이런 이유 때문에 TiO_2 나노 튜브 격자(NTAs)는 전하를 수송 할 수 있는 능력(태양 전지 또는 광전기화학 반응에서 입증됨.), RuO_2 와의 높은 친화성 (치수 안정성 전극에의 응용) 때문에 염소발생반응을 위한 좋은 담지체로 사용될 수 있다. 또한, 나노 튜브 격자는 전기 산화 방법을 이용해 나노 구조를 정밀하게 조절할 수 있으며, 결정성이나 배향, 전기적 특성들을 제어할 수 있다.

이에, 본 연구에서는 최초로 이산화 루테늄을 증착한 이산화 티타늄 나노 튜브 격자를 염소발생반응을 위한 전극으로 제안한다. 나노 튜브 격자는 전기화학적 양극산화방법으로 만들었으며, 열처리 조건에 따른

결정성 및 전기전도도와의 관계를 탐구하였다. 양극 분극 하의 전극의 전도성은 효율적인 염소 발생을 위해 필수적이며, 결함 조절을 통해 양극 분극 하에서의 전도성을 확보하였다. 특히, 아르곤 분위기 하에서 열처리된 나노 튜브 격자를 제조함으로써 흑색 나노 튜브 격자를 제작할 수 있었다. 또한, 이 담지체는 다양한 pH, 넓은 범위의 전압에서 안정적으로 촉매 특성을 낼 수 있는 가장 좋은 전극인 것을 확인하였다.

……

주요어 : 염소발생반응(CER), 이산화티타늄 나노튜브 어레이, 이산화루테늄, 불균일계 촉매, 전기화학적 분석
학 번 : 2016-29604